

**The Blake Ridge:
A Study of Multichannel Seismic Reflection Data**

A Thesis
Presented to
The Academic Faculty

by

Daniel Scott Kahn

In Partial Fulfillment
of the Requirements for the Degree
Masters of Science in the
School of Earth and Atmospheric Sciences


Georgia Institute of Technology
April 2004

The Blake Ridge:
A Study of Multichannel Seismic Reflection Data

Approved by:



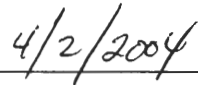
Dr. Daniel Lizarralde, Advisor



Dr. Tim Long

Dr. Robert Lowell

Date Approved



4/2/2004

Acknowledgements

I want to thank to my advisor, Prof. Daniel Lizarralde, for introducing me to the topic of gas hydrates and guiding me through the analysis of the seismic data. I owe a dept of gratitude to the members of the crew and scientific staff aboard the R/V Maurice Ewing 2000, Blake Ridge Cruise for obtaining the data that I used. I also want to express my appreciation to Profs. Robert Lowell and Tim Long for their support and encouragement and for generously serving on my thesis committee.

I am proud to acknowledge the importance of my friends who were always there to lend moral support during the difficult times and shared in my joy during the good times. Liz Donahue, Tatiana Toteva, Sangmyung Kim, Jeff Boyd, Martin Smith, Melissa Geddie, Bill Stewart, Drew Macaulay and Malcolm Campbell, thanks!

**The Blake Ridge:
A Study of Multichannel Seismic Reflection Data**

Daniel Scott Kahn

74 Pages

Directed by Dr. Daniel Lizarralde

The Blake Ridge is a large (~100,000 km²) contourite deposit off the southeast U.S. coast thought to host a substantial reservoir of methane bound as methane gas hydrate and underlying methane gas. In this thesis, we estimate hydrate concentration across the Blake Ridge. A 6-km multichannel seismic (MCS) streamer was used to obtain reflection data. Data from the 44-km length of our regional line across the Blake Ridge enabled a calculation of seismic velocity, determined through the analysis of two-way traveltimes. Hydrate concentration is then estimated from velocity calculations. Substantial methane hydrate concentrations have implications for energy production, climate models, and slope stability. Methane hydrate is a crystalline solid which is stable at temperatures above the freezing point of water. Methane as a hydrate is found within the hydrate stability zone (HSZ) whose depth extent is defined by the phase equilibrium curve. Temperature forbids its formation beneath the HSZ, where a region of free methane gas may exist if local methane concentrations exceed the solubility of the pore fluid. This boundary appears as a bottom-simulating reflector (BSR) in MCS profiles due to the impedance contrast at the boundary between the HSZ and free methane gas. The dependence of the seismic velocity on the hydrate concentration enables the MCS data to yield an indirect measure of sub-oceanic methane hydrate. We fit traveltimes of common midpoint (CMP) reflections at or near the BSR with one-dimensional models. These

models give good fits to velocities and layer thicknesses. Seismic velocities at a depth of 0.46 km below the seafloor range from ~1.70 km/s to ~1.97 km/s, within the HSZ. When the line is examined in the vicinity of the crest, significant changes of velocity with position are calculated. In the flank, there is no significant trend of velocity with position. The hydrate concentration derived from these velocities has an average value over the length of the line of ~7% (hydrate-in-frame) for the three-layer slowness-gradient model at 0.46 km below the seafloor. One-dimensional vertical methane flux models predict a uniform hydrate concentration (Xu and Ruppel, 1999). The significant change of velocity with position near the crest of the ridge in our calculation suggests a lateral methane flux.

TABLE OF CONTENTS

Acknowledgements	iii
Abstract	iv
List of Tables	vi
List of Figures	vii
Chapter 1 Introduction	1
A. Overview	1
B. Methane Hydrate and Methane Gas Formation	3
C. Blake Ridge – Seismic Studies	7
D. Figures	13
Chapter 2 Procedure	16
A. Methodology	16
B. Velocity Models	20
C. Figures	23
Chapter 3 Results	31
A. Overview of Statistical Analyses	31
B. Layer Thickness	33
C. Layer Velocities	35
D. Concentration	39
E. Tables	45
F. Figures	48
Chapter 4 Discussion	61
A. Discussion	61
B. Figures	65
Chapter 5 Conclusions	68
References	69
Vita	74

LIST OF TABLES

Table 3.1	Results for Two-Layer Models	46
Table 3.2	Results for Three-Layer Models	47

LIST OF FIGURES

Figure 1.1	Location of the Blake Ridge gas hydrate province	14
Figure 1.2	Stack MCS sections along Line R22	15
Figure 1.3	Illustrations of structure I and II hydrates	4
Figure 2.1	Residuals with respect to a best-fitting isotropic slowness-gradient model	24
Figure 2.2-2.7	BSR moved-out	25
Figure 3.1	Layer structure along line R22 in the Blake Ridge	49
Figure 3.2	Seismic velocity at 0.46 km below the seafloor along Line R22 calculated in the three-layer slowness-gradient model	51
Figure 3.3	Seismic velocity in the HSZ hydrate along Line R22 calculated in the two-layer constant-velocity model	53
Figure 3.4	The rms difference of the "best picks" from the model traveltime curve	54
Figure 3.5	Constant-hydrate concentration profiles as a function of depth	56
Figure 3.6	Concentration (% volume) of methane hydrate along line R22 in the Blake Ridge	58
Figure 3.7	Change of concentration with depth for selected CMP's	59
Figure 3.8	Differences in concentration from the average for selected CMP's	60
Figure 4.1	Pressure estimated at top and bottom of HSZ	66
Figure 4.2	Phase equilibrium curve for hydrate in seawater with temperature profile for site 997	67

Chapter 1

Introduction

A. Overview

Methane hydrate is a crystalline solid that forms at temperatures above the freezing point of water when a cage of hydrogen-bonded water molecules surround a methane molecule. H. Davy first created gas hydrates in his laboratory in 1811. Engineering interest in hydrates began in the 1930's, when it was determined that gas hydrate formation in pipelines blocked oil and gas. Naturally occurring methane hydrate was originally discovered in sub-surface sediments in the Siberian permafrost in 1964, and subsequently hydrate deposits were found in the ocean sediment of continental margins (Sloan, 1998). Since then, increasing evidence suggests that there is a global abundance of methane hydrate and free gas in the shallow geosphere (Kvenvolden, 1993). Methane hydrate has been recovered at 19 sites worldwide and inferred in another many more from geophysical and geochemical methods (Kvenvolden and Lorenson, 2001). The unique properties of methane and the size of the sub-oceanic reserves have attracted researchers' interest.

Globally distributed methane hydrate is of interest for several reasons. Methane hydrate represents a potential future source of energy. Estimates of the global volume of methane trapped in hydrate structures vary by over three orders of magnitude from 3,114 to 7,634,000 trillion cubic meters (Kvenvolden, 1993; Kvenvolden et al., 2001). This can be compared with the remaining recoverable methane gas reserves of 250 trillion cubic meters (Masters et al., 1991). The sub-oceanic concentrations of methane represent both a source and sink in the global carbon cycle (Dickens, 2001). The direct transfer of

methane from these reserves into the atmosphere can effect global climate because methane is an efficient greenhouse gas (Dillon, 1992; Dickens, 2001). Furthermore, the existence of hydrates in sediment layers can affect the physical properties of the seafloor and cause slope instability; sensitivity of hydrates to pressure and temperature can cause them to dissolve with only slight changes in these parameters. The resulting slides or collapses can have detrimental effects on drilling, seafloor pipelines, and heavy structures (Dillon, 1998). There is even speculation that catastrophic release of methane could trigger tsunamis (Bugge et al., 1987; Nisbet and Piper, 1998; Laberg et al., 2000).

Understanding the dynamic controls on methane distribution within a methane gas hydrate regime is key to determining the role of hydrate in the global carbon cycle and in assessing methane hydrate's potential impact on slope stability and future energy needs. The processes involve the balance of methane production, transport, and release into the ocean and atmosphere. Our current understanding of these controls is embodied in a 1-D flow/flux model which balances *in situ* methane production with compaction driven fluid flow (Xu and Ruppel, 1999; Wood and Ruppel, 2000; Rempel and Buffet, 1997). The 1-D flow of methane depends upon the balance between the *in situ* production and the sedimentation rate. If, for example, the sedimentation rate is low and the *in situ* production is high, it is expected that the methane would begin to saturate the pore space. A vertical flow of methane results from the compression of sediments by the overburden exerted by additional sedimentary deposits. Whether methane flux is predominantly limited to one-dimensional flow or has a significant two, and three-dimensional character is the subject of study. Two and three-dimensional flows involve high-permeability

pathways through the strata which tend to redirect the flow regime. (Holbrook, 2001; Davie and Buffet, 2001).

The data for this project was acquired during RV *Maurice Ewing* cruise number EW0008 to the Blake Ridge in 2000, using a multichannel seismic (MCS) 6-km-long streamer. The main goal of the cruise was to conduct a site survey for a drilling proposal of a "collapse" feature near the crest of the ridge that was thought to be linked to a catastrophic release of methane gas into the ocean and possibly the atmosphere. An outcome of the survey was that, in fact, no collapse had occurred. A supplementary study involving 40- to 60- km long, regional, MCS lines was carried out to examine the distribution of hydrates using detailed velocity analysis. One of these regional lines, Line R22, was the focus of this thesis. Line R22, which traverses the Blake Ridge along the ODP Leg 164 drilling transect (Figures 1.1 and 1.2), spans approximately 44 km. This thesis analyzes MCS reflection data to determine velocities that are then used to estimate hydrate concentration. From these concentrations inferences about the dynamic controls which govern methane distribution are made.

B. Methane Hydrate and Methane Gas Formation

Hydrates are crystalline structures composed of water-lattice cavities filled with foreign gases, in this case, methane. These structures are held together by Van der Waals forces under modest pressures and low temperatures. The methane gas is required to support the cavity that the water lattice has left vacant. Other gases can occur in this form, but in the natural environment methane hydrate is the most prevalent.

In nature there are two pertinent structures of hydrates, structure I and structure II, with 3 types of cavities (Sloan, 1990; Jeffrey and McMullan, 1967). The three types of cavities are pentagonal dodecahedron, 5^{12} , where 5 indicates the number of edges, and 12 represents the number of faces; a tetrakaidecahedron, $5^{12}6^2$ (12 pentagonal faces and 2 hexagonal faces); and a hexakaidecahedron, $5^{12}6^4$. Structure I hydrates are formed from a combination of 5^{12} and $5^{12}6^2$ cavities while structure II hydrates are formed from 5^{12} and $5^{12}6^4$ cavities. These hydrates contain proportionally large amounts of methane. For example, in a structure I hydrate the ratio of water molecules to guest molecules in methane hydrate is $1:5\frac{3}{4}$ (Kvenvolden, 1993).

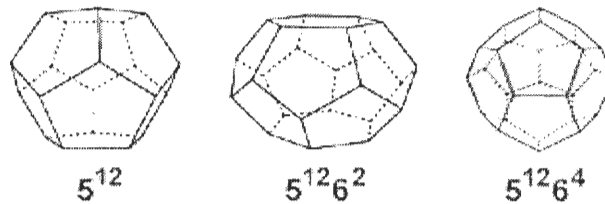


Figure 1.3 Illustrations of structure I and II hydrates (Courtesy of the Centre for Gas Hydrate Research at Heriot-Watt University).

Methane hydrate occurs in two typical types of sedimentary environments: clay-rich, high porosity, ocean-bottom sediments and subarctic and arctic onshore sands. The first environment will be the focus of this paper because of the location of the Blake Ridge (Figure 1.1).

The formation of methane hydrate is sufficiently complex, that only recently have pure samples of sufficient size for acoustic studies been made in the lab (Helgerud, 2001). For hydrate to form, methane gas must move into the hydrate stability zone (HSZ), where temperatures and pressures enable formation in the presence of water. It

has been postulated that before natural hydrates can nucleate, the pore water has to be fully saturated with methane; the amount of methane that exceeds the saturation level is free for hydrate formation (e.g Sloan, 1990; Paull et al., 1994; Brooks et al., 1994).

Two processes exist which produce the substantial amount of methane that exists beneath the seafloor: a thermogenic and a biogenic process. The thermogenic process of methane production relies on a breakdown of more complex hydrocarbons. This is a common process in the formation of hydrocarbon gases (e.g Hunt, 1979). The biogenic process, on the other hand, depends primarily on the activity of bacteria.

In the thermogenic formation of methane, methane is created in a series of three phases: diagenesis, catagenesis, and metagenesis (Tissot, 1997). Diagenesis takes place in the shallow subsurface and begins during initial deposition and burial (North, 1985). These shallows range from 0-1000 meters deep and from $\sim 0^{\circ}$ to 60° C. The principal process that is at work is decay of organic material aided by bacteria. The products which are produced are methane, carbon dioxide, water, kerogen (solid, insoluble, organic matter, consisting predominantly of algae and woody plants), and bitumen (inflammable organic matter, including asphalt and mineral wax) (North, 1985). The proper temperature is crucial for this process to move forward because of the sensitivity of bacteria to temperature changes. The bacteria die off with increasing depth of burial as a result of the increase in ambient temperature. While bacteria produce large amounts of methane as a by-product during diagenesis, the rate of methane production eventually falls off as the temperature increases. The catagenesis phase therefore becomes much more dominant during the deeper burial.

Catagenesis is a thermodynamic, nonbiogenic process by which kerogens are broken down to smaller hydrocarbons. The ranges for this phase are from 1000-6000 meters and 60-175° C. During catagenesis, kerogen is changed into petroleum through a process whose rate is controlled by temperature and pressure (Tissot and Welte, 1984). The catalysts are usually surfactant minerals in sulfurs and clays. Above 60° C, oil starts to form, thus, this temperature is called the critical oil temperature (North, 1985). The increase in temperature occurs because of burial depth and its relation to the geothermal gradient. Once the catagenesis phase produces temperatures above 200° C all the hydrocarbons are converted to methane and graphite, although this is a slow process.

The final phase is metagenesis. This process occurs at extremely high pressures and temperatures that parallel metamorphism. In this stage, the majority of the hydrocarbon released from the kerogen is methane. From that point forth the H:C ratio declines until graphite is the only residue remaining.

The second process for the production of methane is biogenic formation. Biogenic formation is crucial for the production of large quantities of methane during the first phase of diagenesis. As the name implies, biogenic methane formation involves microbial organisms that decompose the material to produce methane. All organic matter is assumed to have the elements carbon, nitrogen and phosphorous contained within them. For example, in phytoplankton carbon, nitrogen and phosphorus appear in roughly the ratio of 106:16:1, known as the Redfield ratio (Redfield,1963) (See formula below.). Biogenic formation is sectioned into 6 stages as characterized by Sloan (1990): oxidization, nitrate reduction, sulfate reduction, carbonate reduction (where methane is initially produced), fermentation, and thermogenic processes. Redfield (1963) postulated

a formula to describe the biogenic formation of methane: $(\text{CH}_2\text{O})_{106} (\text{NH}_3)_{16} (\text{H}_3\text{PO}_4) \rightarrow 53\text{CO}_2 + 53\text{CH}_4 + 16\text{NH}_3 + \text{H}_3\text{PO}_4$.

C. Blake Ridge - Seismic Studies

The Blake Ridge is a gas hydrate reservoir that has been the target of many studies. It is a physiographic feature formed as a contourite drift deposit of marine sediments resulting from deep-ocean contour current interaction off the southeast margin of North America (Mountain and Tucholke, 1985) (Figure 1.1). The Blake Ridge has several advantages that have encouraged investigations of gas hydrate, free gas distribution, and the processes that occur during the evolution of gas hydrate. First, the Blake Ridge has both lateral and vertical homogeneity of sediments and sedimentary processes, which enable changes in seismic stratigraphy and seismic velocity to be directly correlated with the presence of methane gas hydrate or free gas (Holbrook, 2001). Also, the Blake Ridge is located away from any tectonic activity so methane hydrate and gas distribution is controlled by *in situ* production and compaction driven flow. Finally, the Blake Ridge has a well-defined bottom-simulating reflector (BSR) which suggests regional abundance of methane gas and hydrate (Shipley, 1979; Dillon et al., 1998; Holbrook, 2001; Paull et al., 2000).

The BSR in general coincides with the base of the hydrate stability zone (HSZ) and is indicative of the phase boundary between methane hydrate and the underlying free methane gas beneath ridge structures. For some time there were two competing BSR models. The first concluded that the BSR was caused by the seismic impedance contrast between the top of the gas layer and the bottom of the hydrate layer (Shipley et al. 1979;

Paull and Dillon, 1981). The second postulated that the BSR was formed from the impedance contrast between the underlying sediments containing an anticipated low velocity and the overlying sediments containing a high velocity methane hydrate. The BSR is now understood to be the reflector at the top of the free methane gas zone, in agreement with early speculations (Shipley et al. 1979; Paull and Dillon, 1981). Seismic research has shown that the BSR is characterized by large negative reflection coefficients indicating that methane gas is present below the hydrate (Shipley et al., 1979; Millar et al., 1991; Hyndman et al., 1992). The bright reflection is caused by the presence of the trapped gas rather than a high concentration of methane hydrate above the BSR (see for example: Katzman 1994; Holbrook et al., 1996; Singh Minshull, 1994; and Holbrook, 2001). Since the thermodynamic boundary conditions (density, pressure, and temperature) are determined to a large extent by the depth below the seafloor, the BSR tends to parallel the seafloor.

The strength of the BSR varies substantially over the ridge, as evidenced in Figure 1.2. This variability suggests a lateral variability methane flux across the Blake Ridge and, thus, perhaps hydrate. Most studies of the Blake Ridge have been focused near the peak of the ridge where the BSR is the brightest (Taylor et al, 1999). In this thesis, we examine velocity profiles derived from MCS data to get estimates of methane hydrate concentration laterally across the Blake Ridge and discuss the implications that position dependent concentrations have for lateral methane flux.

Sediments in which methane hydrates replace part of the pore fluid have higher seismic velocities than sediments in which the pore fluid is made up of seawater (Helgerud, 2001). However, when methane hydrate is a sediment frame component, it

has a stronger impact on the velocities than when it is part of the pore fluid because of its effect on sediment elastic properties (Helgerud, 2001). Detection of methane gas and methane hydrate can therefore be accomplished through seismic analysis. The relatively uniform lithology of the Blake Ridge enables variations in velocity to be associated with the occurrence of hydrate or gas (Holbrook, 2001). This makes the velocity analysis of a specified area a reliable technique to estimate the distribution of methane hydrate throughout the structure.

There are several principal sources for seismic velocity data on the Blake Ridge:

- a) downhole sonic log measurements – these present very accurate measurements at high frequencies, are used at ODP Legs 994, 995, and 997 (Taylor et al., 1999).
- b) vertical seismic profile (VSP) data –agree quite well with downhole sonic logs, except at drill site 997 where large variations in velocities occur (Holbrook et al., 1996)
- c) ocean-bottom seismic data (OBS)– wide angle reflection data recorded on hydrophones on the ocean bottom (Katzman et al., 1994)
- d) interval velocities from a few multichannel seismic reflection lines. (Ecker et al., 2000)

A sample of results is presented below.

Helgerud (2001) used data from the Ocean Drilling Project 164 to model compressional wave speeds at site 995. Core porosities varied from 0.7 (at 200 meters beneath the seafloor) to 0.55 (at 450 meters beneath the seafloor). Over the same depths velocities went from ~1600 m/s to ~1900 m/s with the maximum just above the BSR.

This yields a peak bulk hydrate concentration of 10 to 15% (at ~450 mbsf) for hydrate as a sediment frame component or in the pore fluid, respectively.

Holbrook(2001) analyzed and compared VSP and OBS results to determine the cause of the discrepancy between the two. His interpretation of the VSP data, using the effective medium model of Helgerund (1999) led him to the conclusion that bulk hydrate concentrations are near zero at 200mbsf and increase with depth toward the BSR, reaching about 4-5% for hydrate-cement model and 14% for the hydrate as a fluid model (Holbrook, 2001). His reanalysis of Korenaga et al's (1997) OBS data yielded peak velocities of 2.15 km/s compared to Korenaga's 2.32 km/s, reaffirming the existence of a high speed wedge just above the BSR, at least at site 997. The disparity between the velocities found from VSP (~1.9 km/s) and OBS arose from anisotropy in which the P-wave velocity was faster along the layer than it was perpendicular to it. This is referred to as transverse isotropy. VSP yields velocities in the vertical direction, which is primarily perpendicular to the layers, while OBS are wide-angle detectors and respond to horizontal as well as vertical waves. This has implications for the determination of the concentration since it is determined from the velocities (9% at 1.9km/s and 14% for 2.15 km/s). Holbrook (2001) suggested that an "equivalent isotropic" velocity, somewhere between the VSP and the OBS values, is the best one to use. Helgerud (1999) has found a systematic transverse isotropy of about 6% from a similar analysis.

With this array of data sources, the abundance of methane hydrate in the Blake Ridge has yet to be precisely determined. The combined amount of methane in hydrates and in free gas beneath the HSZ in the Blake Ridge is calculated to be 70 trillion cubic meters of gas over an area of 26,000 km² (Dickens et al.,1997), 57 trillion cubic meters

(including free gas) over 26,000 km² (Collett and Ladd, 2000) and about 80 trillion cubic meters of gas for an area of 100,000 km² (Holbrook et al., 1996). Other studies suggest that the methane hydrate at the 3,000 km² peak of the ridge may have 18 trillion cubic meters of methane gas (Dillon and Paull, 1983). Sloan's survey (1999) finds a 1-5% bulk sediment is filled with gas hydrate throughout an ~250 meter thick section. This value is extrapolated over 24,000 km² to yield a reserve of 38-80 trillion cubic meters of gas.

The great variance in these estimates depends upon the method that was used for measurement. For example Dickens used the free methane measured from core samples, while Holbrook depended upon vertical seismic profile data from boreholes. "One of the most critical scientific problems is the need for accurate determination of the occurrence, distribution, and concentration of gas hydrates in nature." (Sloan et al., 1999).

The lateral variation of the concentration of methane hydrate is the crux of this thesis. The methane hydrate concentration as a function of the distance from the crest of the ridge can be determined by examining the velocity profile over the full length of Line R22. Because of the uniform sedimentation throughout the Blake Ridge (Paull et al., 1996), a model with dominant vertical methane transport would predict a uniform distribution of hydrate. Regional concentrations of methane hydrate, which are determined by *in situ* methane production and methane flux, can therefore be used to estimate the relative importance of lateral migration of methane. This lateral transport of methane could be an influential factor in the formation of methane hydrate. An increase in the relative importance of two-dimensional methane gas flux from that commonly acknowledged (Wood and Ruppel, 2000; Xu and Ruppel, 1999; and Gorman et al., 2002)

could cause a revision in our understanding of the role of high-permeability pathways with significant lateral components.

D. Chapter 1 Figure Captions

Figure 1.1

Location of the Blake Ridge gas hydrate province. Line R22 is shown along the NE-SW direction with ODP sites 994, 995, and 996 indicated. The dashed line indicates the extent of the province (from Dillon et al, 1995).

Figure 1.2

Stack MCS sections using SIOSEIS along Line R22 (program courtesy of Paul Henkart). The strength of the BSR is larger beneath the crest, suggesting a greater accumulation of free methane gas. The positions of boreholes 994, 995, and 997 are labeled. The arrows correspond to the locations of the CMP's that are displayed in Figures 2.2-2.7.

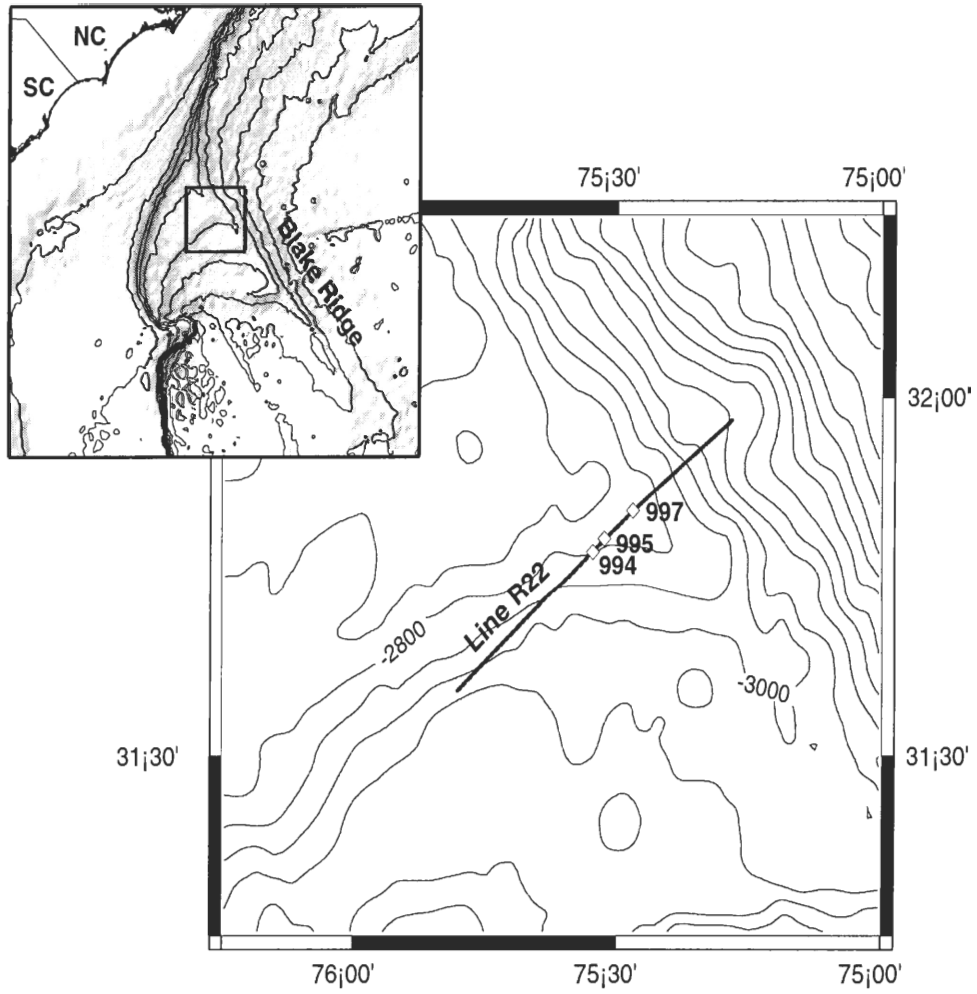


Figure 1.1

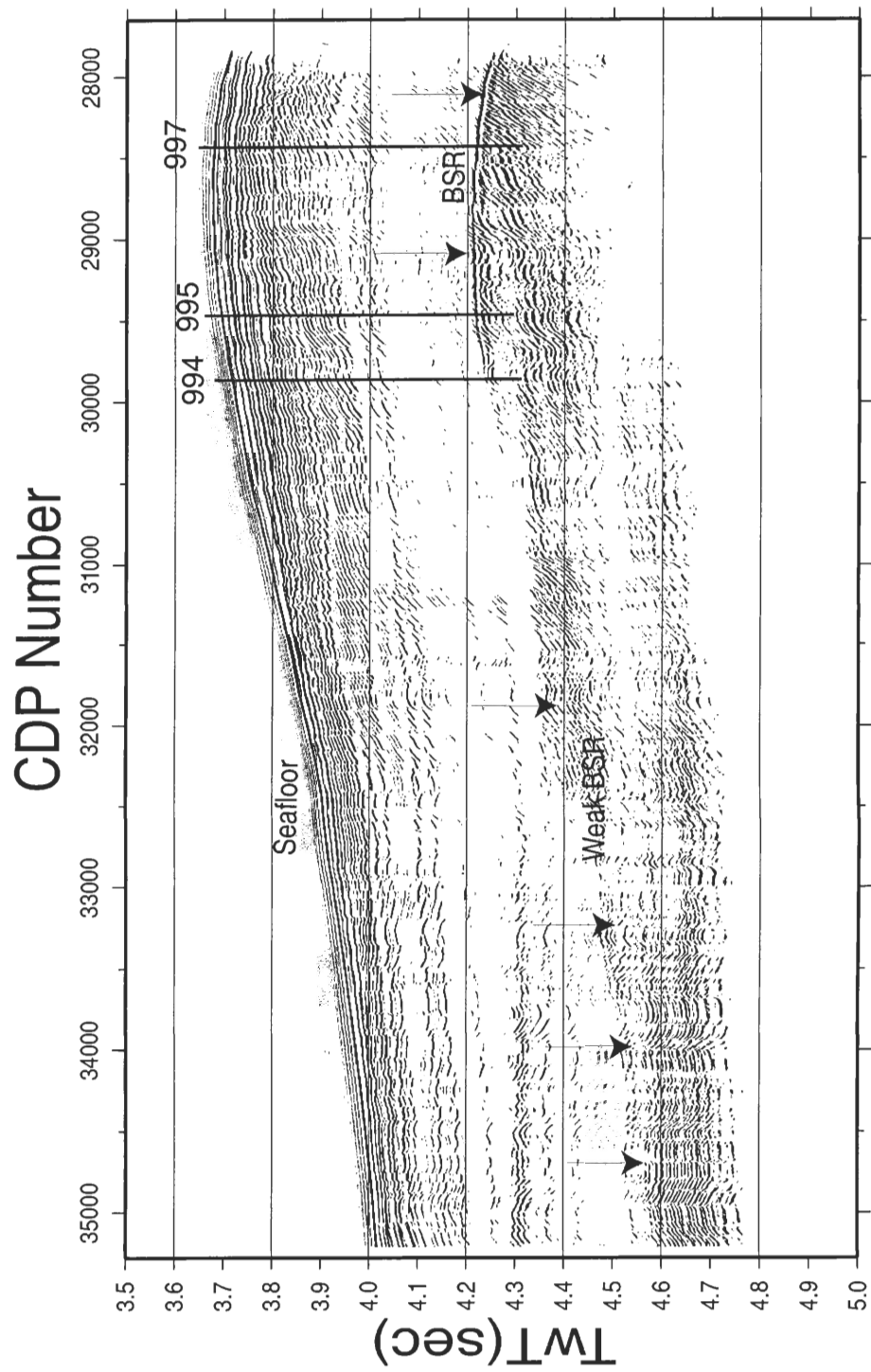


Figure 1.2

Chapter 2

Procedure

A. Methodology

The goal of the project is to use the velocity and derived concentration of hydrate to determine the lateral variability of methane hydrate, and from that infer the methane flux along the line. In this section, we describe how the parameters describing a multi-layer model for Line R22 on the Blake Ridge are determined from MCS data.

Seismic velocity can be obtained from the moveout of reflections observed on a set of equally spaced hydrophones, attached to a 6-km MCS streamer, extending in a nearly straight line with the airguns at one end. Moveout is the delay in the reflection traveltimes from zero offset, corresponding to vertical reflection, to the nearest hydrophone, which increases as the source-receiver distance increases. As the ship moves forward shots are fired at regular intervals. The hydrophones receive acoustic signals sourced by the airguns, after reflecting from layer boundaries. The reflection data are recorded as traces, which give the time-dependent acoustic signal, magnitude and phase, for a specific offset. Traces from various source-receiver combinations are collected into a common-midpoint (CMP) gather, a set of traces with a common reflection point, from multiple shots, with varying horizontal ranges between source and receiver. A CMP gather allows traveltimes to be viewed in 1D with no lateral variation, allowing complex structures along a "line" to be imaged. The analysis throughout this thesis is based on 1D traveltimes modeling of individual CMP's.

The streamer geometry provides a length scale which is used to interpret the data. Groups of six hydrophones are spaced every $\Delta x=12.5$ meters. The streamer and airgun move by intervals equal to approximately 32 meters between shots. Ideally, this distance is a multiple of the CMP spacing, so that the hydrophones will be in equivalent locations with each shot. The distance between CMP's is half the spacing of the hydrophones equaling 6.25 meters. There are 480 channels or groups; however, each CMP in the current data has a maximum of 80 traces spaced 75 ($= 6*\Delta x$) meters apart. The moveout between these traces is the input for the determination of the velocity model.

The data used to constrain the velocity models are reflection times, and so the traveltimes are picked from the original unstacked data. The traveltime that is measured is the time that the acoustic signal takes to travel from the source to the receiver propagating through the media while being reflected and refracted at impedance contrasts. Traveltime "picks" refer to the time to the reflection event of interest, as denoted by the signal onset, on selected traces. Our picking methodology involves the following steps. We choose to analyze every 8th CMP as a compromise between precision and processing time. Traveltime picks are made by hand on about 10 traces for each of these CMP's. These selected X-T pairs are then used to determine an initial velocity model, which enables the calculation of a model traveltime curve.

The initial velocity model is obtained by calculating the depth of the reflecting layer, z , and the acoustic speed, v , in each layer, which minimizes the root mean-square (rms) error between the initial picks and the calculated travel time. The determination of the best velocity and depth uses a grid search over a range with incremental

$dv=0.0001\text{km/s}$ and $dz=0.0001\text{km}$ until the minimum value of rms error is found. The resulting velocity and depth define the model. That is

$$\sum_{i=1}^{i=n} (T_{pick,i} - T_{pred,i})^2 \quad (2.1)$$

is minimized, where the sum, is over n picked traces. $T_{pred,i}$ is calculated by the traveltine equation,

$$T_{pred,i} = Xp + 2 \sum_j Z_j q_j \equiv Xp + \sum_j \tau_j \quad (2.2)$$

where the offset X is given by,

$$X = 2p \sum_j \left\{ Z_j \frac{\sqrt{(u_j^2 - p^2)}}{(u_j^2 - p^2)} \right\} \equiv p \sum_j \frac{\tau_j}{(u_j^2 - p^2)} \quad (2.3)$$

Here Z_j is the thickness of layer j , $p=u_j \sin(\theta)$, the ray parameter, and $q_j=u_j \cos(\theta)$, with $u_j=1/v_j$, the slowness, and X , the offset, is the horizontal distance between the source and receiver.

The initial velocity model based on the hand picks is used to generate predicted times for each trace. These predicted traveltimes are used to define a tapered window about the reflection event of interest. The windowed data are then used as input to a cross correlation based automatic picking routine. The cross correlation is a measure of coherence between two seismic traces,

$$c_i(\tau) = \sum_{j=1}^n S_i(t_j) S_{i+1}(\tau - t_j) \quad (2.4)$$

where S_i and S_{i+1} are adjacent traces. The sum is over the time window, and τ is a lag time. We found the lag time that maximizes the cross correlation, $c_i(\tau)$. If the cross correlation is not greater than a specified threshold, then the trace is flagged as being non-coherent. A bad trace will have a low cross correlation with the trace before and the trace after it. Furthermore, if the lag time for the maximum correlation is greater than twice the lag for the predicted time, the trace will also be flagged. A value from the predicted traveltimes equation is then substituted for flagged values. The "best picks" are found by running the lag curve through all the initial picks and then averaging the lag curves on each trace.

This process results in a more accurate set of traveltimes picks. The new velocity model therefore has the ability to achieve an even smaller uncertainty in calculating a 1D traveltimes curve. Figure 2.1 shows a comparison of the residuals, for BSR traveltimes with respect to a best-fitting slowness gradient isotropic model, between the hand picks and the cross correlation picks. The resulting rms error for each CMP is found to be on the order of 6×10^{-4} s. The "best picks" traveltimes are used to produce a final velocity model, following the same method as described above. Figures 2.2 to 2.7 display the BSR reflection moved out to the "best picks" and the best fit model for selected CMPs. To avoid errors resulting from potential non-linearity at the ends of the streamer, the offsets were limited to a range between 0.5 and 5.5 km. In part (a) of these figures, the deviation of the onset of the signal from 0 is indicative of picking "errors," while in part (b) the deviation comes from model "errors."

B. Velocity Models

We consider three main velocity models in this thesis: a constant velocity model, a linear-gradient slowness model, and an anisotropic velocity model. For the constant velocity model, the velocity associated with each CMP is the average velocity in the layer which gives a best fit to the data. The constant velocity model should give a reasonably good fit to the known layer structure. However, since data from borehole measurements (Holbrook, 2001) taken at the Blake Ridge (site 995) indicate that the velocity increases with an approximately linear dependence on depth in the HSZ, as an obvious result of compaction, a linear slowness-gradient model is the next logical step. The contrast in velocities between vertical seismic profiles and ocean bottom hydrophones demonstrates that anisotropy is also present in the HSZ (Holbrook, 2001). Transverse isotropy in the HSZ is approximated in the anisotropic velocity models.

These models are applied to two- and three-layer structures, in which the three-layer structure includes separate modeling of a constant-velocity sediment layer overlying the HSZ, in addition to the seawater layer. The two-layer model describes the basic structure of the system and is expected to provide approximate values for the layer thicknesses and velocities. The sediment layer was separated from the HSZ because no methane hydrate is likely to be present in this depth range, thus, it is thought to bias the HSZ velocity calculated in the two-layer model (Holbrook, 2001).

The procedure for determining the model parameters follows that described above, a grid search followed by a cross-correlation calculation, to arrive at the "best

picks." The "best picks" are then used to determine the model velocity and thickness through the travelttime equation, re-employing the grid search.

In the slowness-gradient model, $u = u_0 + gZ$, the time and the offset need to be integrated over the depth. The results of the integrations are

$$\tau = \left(\frac{u_0}{g} + Z_j \right) \left[\left((u_0^2 - p^2) + 2u_0gZ_j + g^2Z_j^2 \right)^{1/2} \right] - \left(\frac{u_0}{g} \right) (u_0^2 - p^2)^{1/2} - \left(\frac{p^2}{g} \right) \ln \left\{ \frac{[u_0 + gZ_j + [(u_0^2 - p^2) + 2u_0gZ_j + g^2Z_j^2]^{1/2}]}{[u_0 + (u_0^2 - p^2)]^{1/2}} \right\} \quad (2.5)$$

and

$$X = \left(\frac{2p}{g} \right) \ln \left\{ \frac{[u_0 + gZ_j + [(u_0^2 - p^2) + 2u_0gZ_j + g^2Z_j^2]^{1/2}]}{[u_0 + (u_0^2 - p^2)]^{1/2}} \right\} \quad (2.6)$$

Equations (2.5) and (2.6) can be used to determine the model through two procedures.

The slowness at the top of the HSZ, u_0 , can be assigned and that value used to calculate a lower boundary slowness, u_L , and a thickness, z . Alternatively, a fixed gradient g_j can be used to calculate values for u_0 , u_L , and z . The method we choose is to assign an upper boundary slowness of slightly larger magnitude than the slowness in the overlying layer.

In the previous discussion it was assumed that the seismic velocity in the layers is isotropic; that is, the velocity is independent of direction. However, as mentioned in the previous chapter, there is evidence for anisotropy in the form of transverse isotropy. We

account for this by approximating the transverse isotropy through weighting the horizontal slowness in eq. (2.2) as $p'=p(1-\alpha)$, where α is the anisotropy parameter. Note that this parameterization is only used in the HSZ layer where the anisotropy is expected to be most pronounced.

C. Chapter 2 Figure Captions

Figure 2.1

Residuals with respect to a best-fitting isotropic slowness-gradient model for BSR traveltimes for CMP 28154. Light dots are the cross-correlation picks; dark dots are hand picks.

Figure 2.2-2.7

BSR moved-out to a) cross-correlation picks and b) best fit model, for a selection of CMP's. Deviations from the zero line are indicative of picking "errors," believed to result from weak reflections crossing the BSR and generating phase shifts.

Residual of CMP 28154

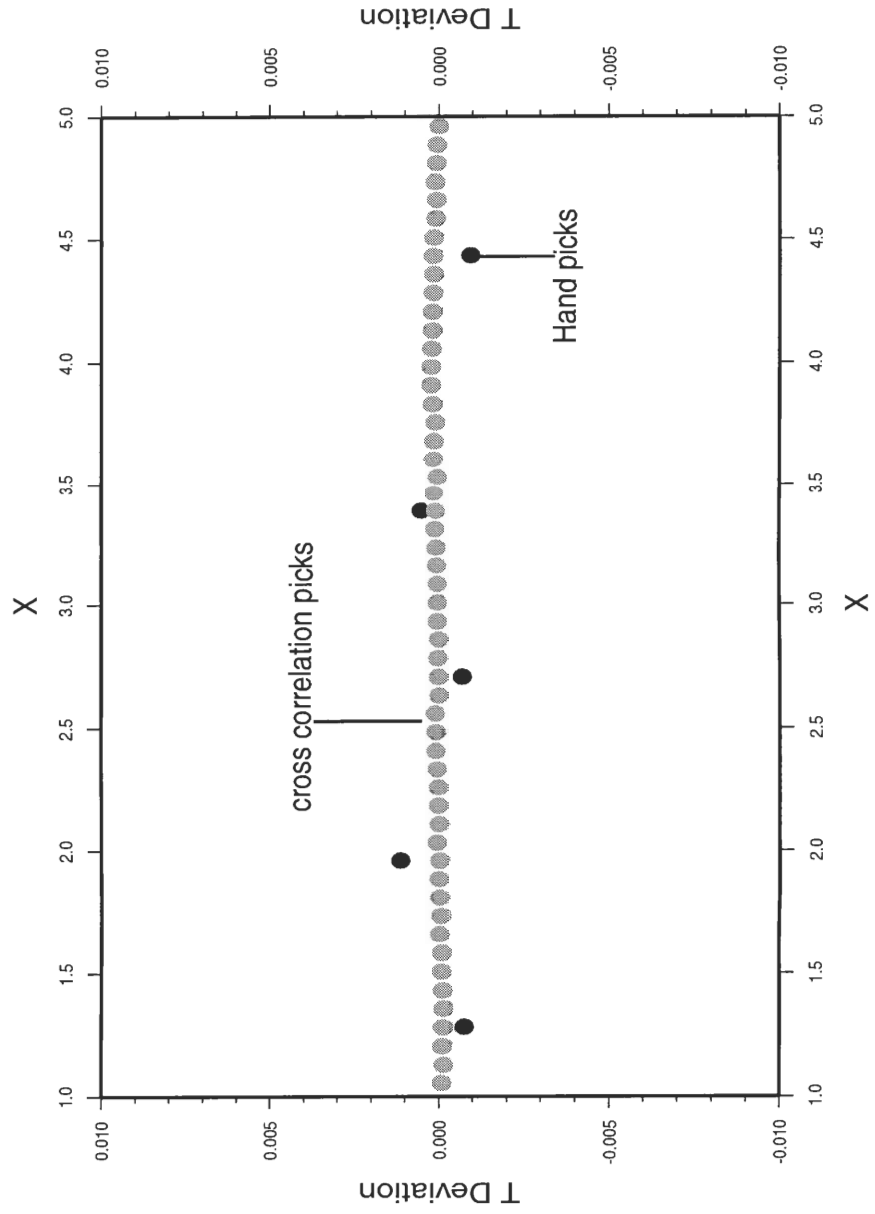


Figure 2.1

CDP 28154

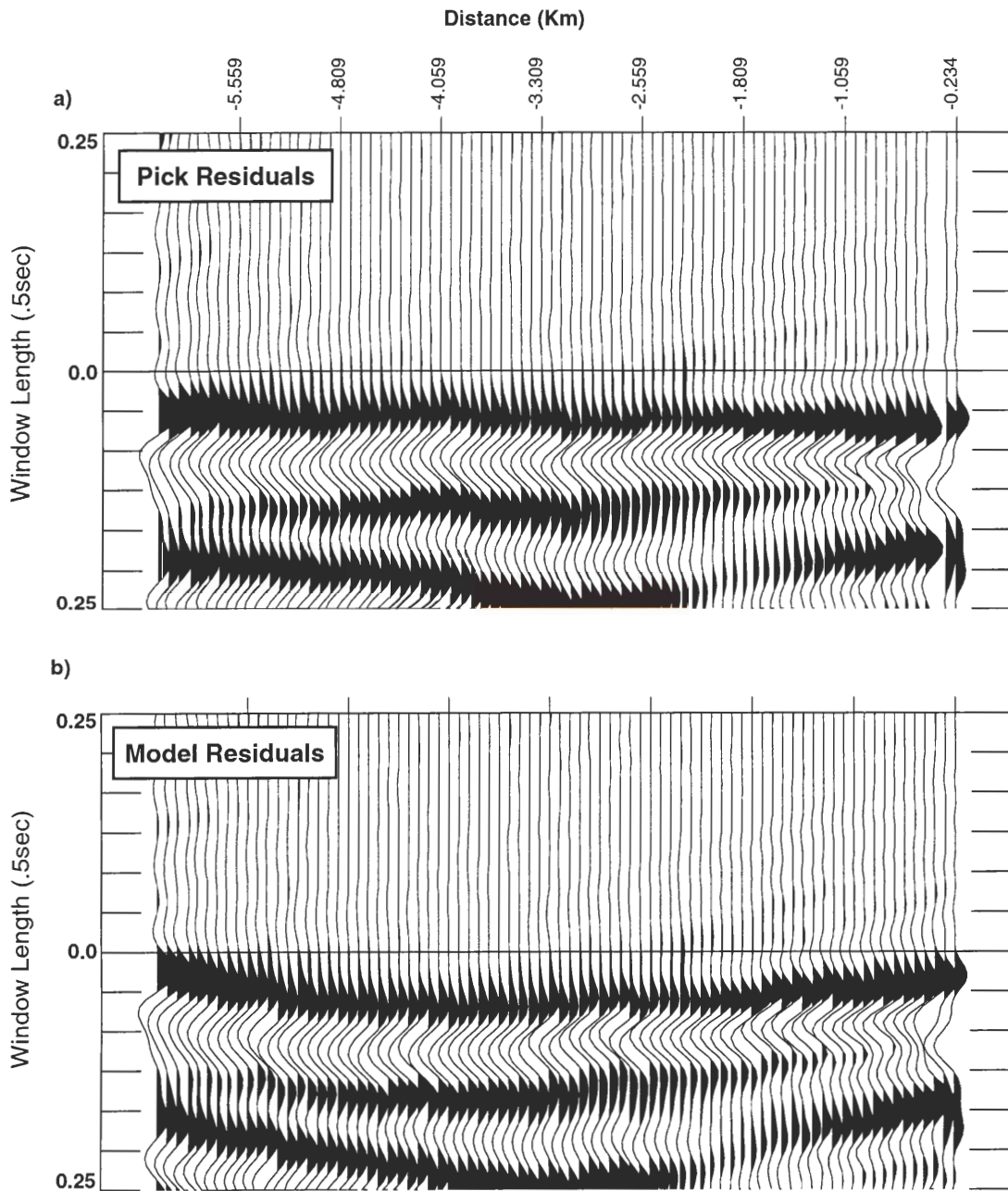


Figure 2.2

CDP 29154

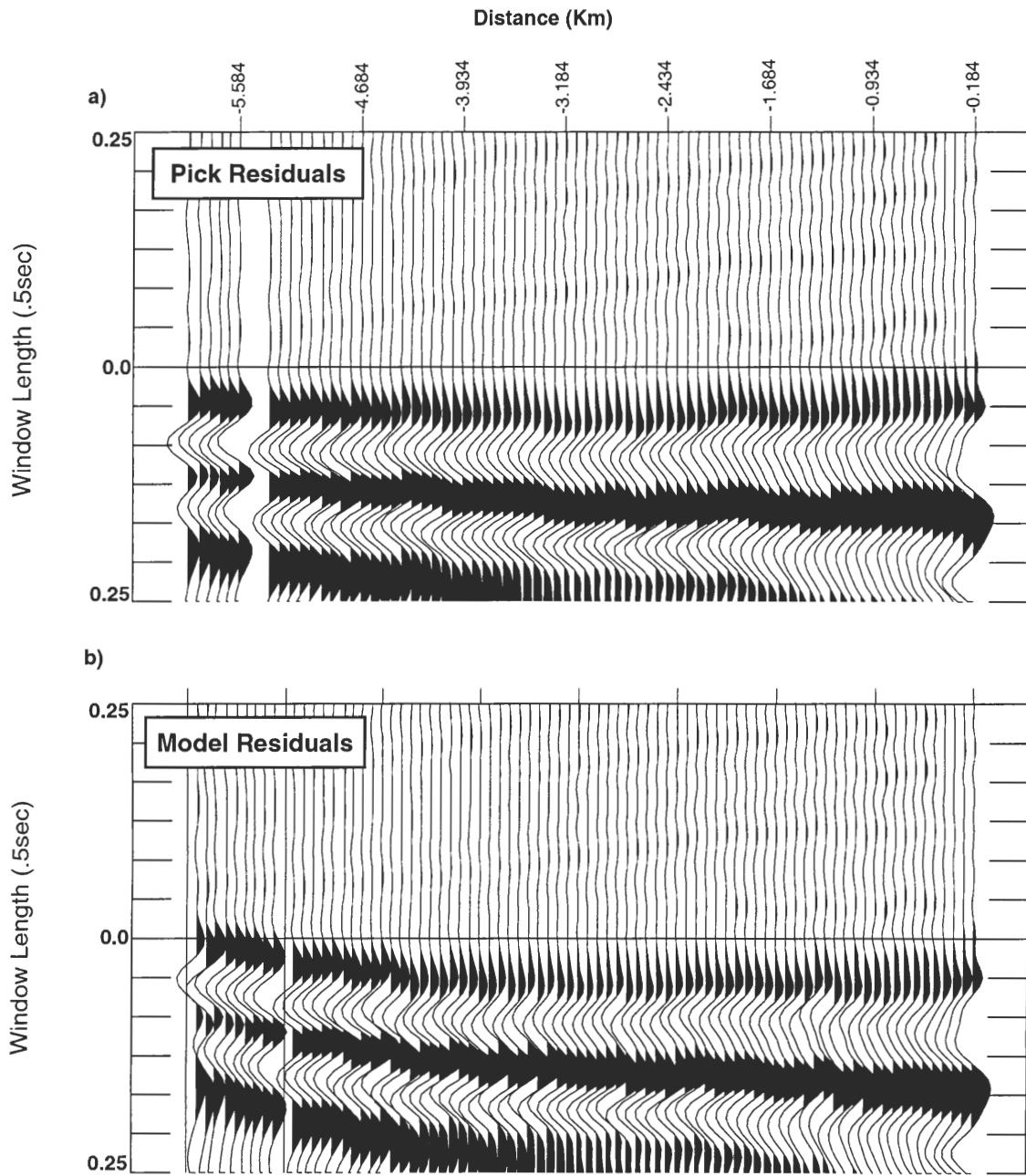


Figure 2.3

CDP 31907

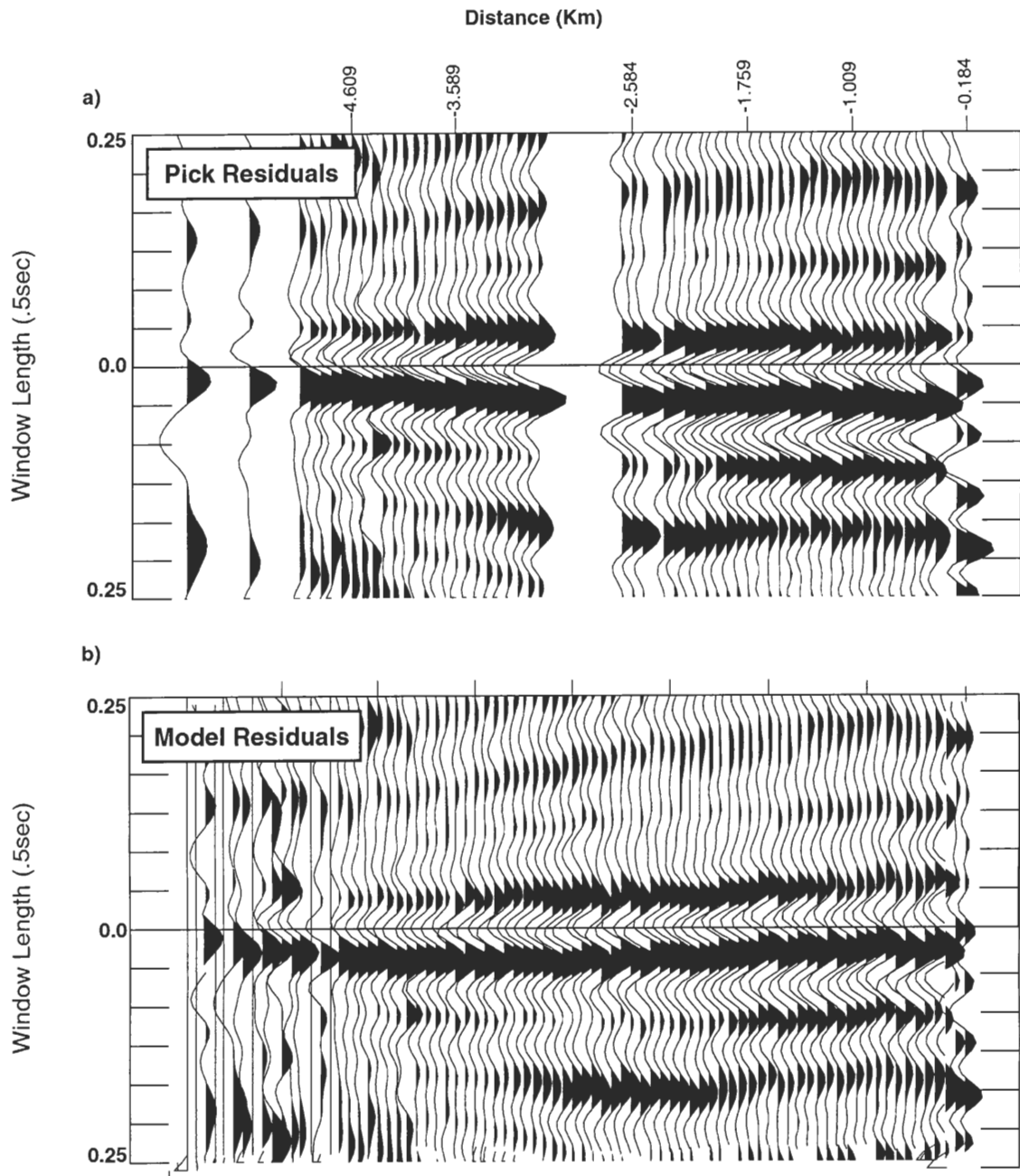


Figure 2.4

CDP 33243

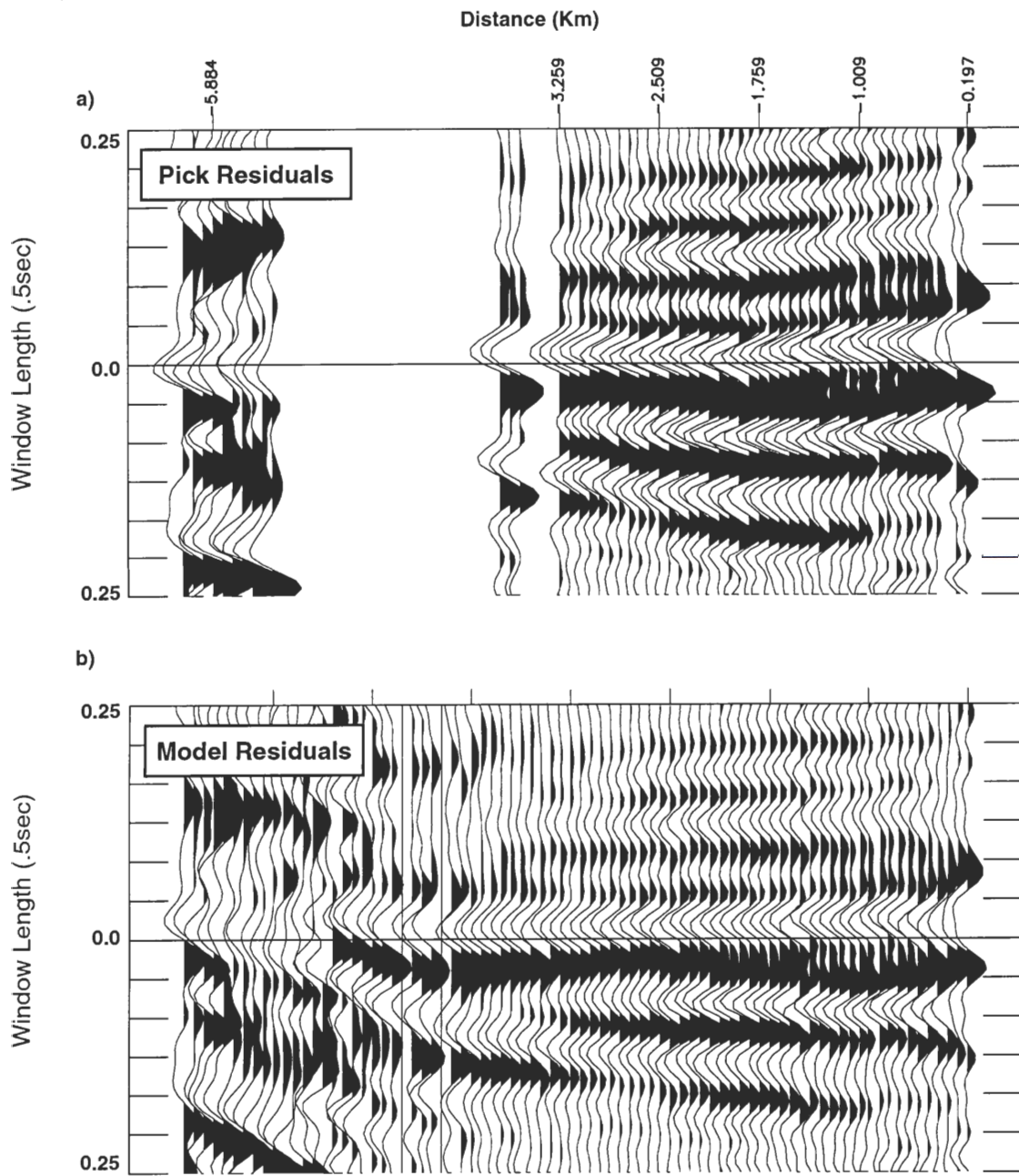


Figure 2.5

CDP 34003

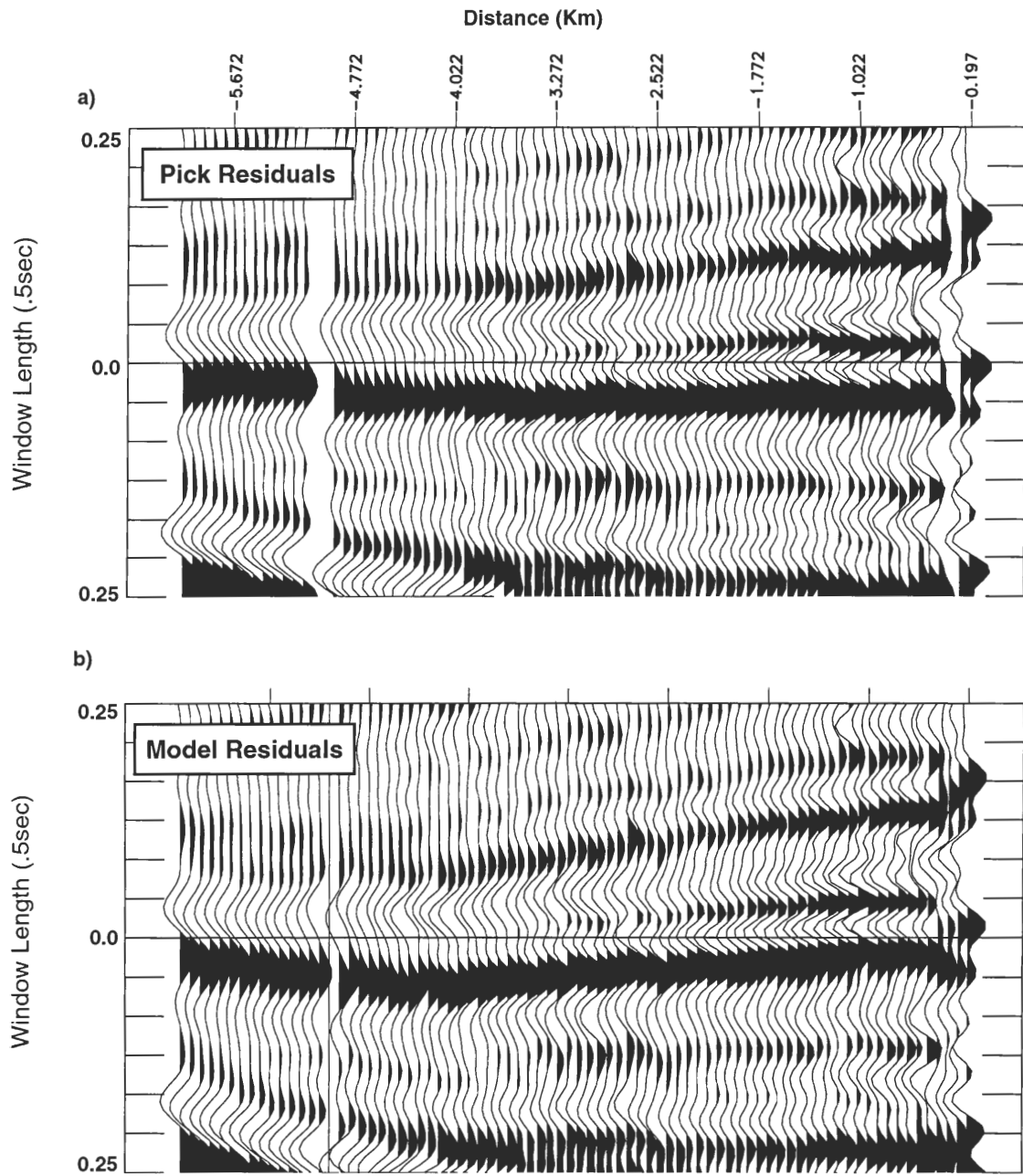


Figure 2.6

CDP 34683

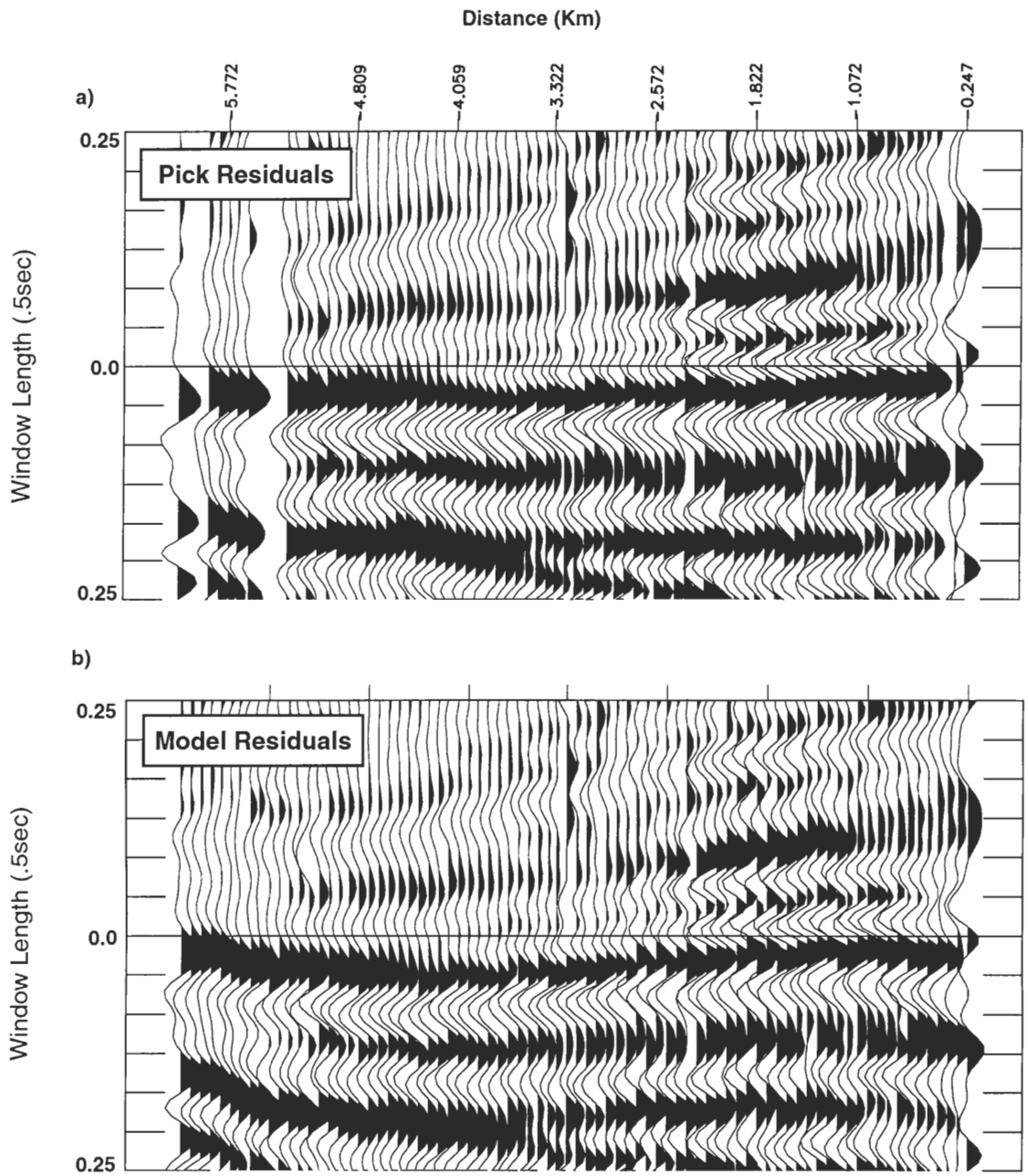


Figure 2.7

Chapter 3

Results

The results in this chapter include p-wave acoustic velocities in the layers (seawater, sediment, and HSZ), the thickness of the layers, and the resulting estimates of the concentration of methane hydrate in the HSZ. The models used to determine these results were two-layer models (seawater and HSZ), with constant velocity and slowness gradient profiles, and three-layer models with and without anisotropy.

A. Overview of Statistical Analyses

The uncertainty and the significance of the results, their average values as well as their dependence on location, as determined by a slope (with respect to CMP) from linear regression analysis, are calculated. The uncertainties that are quoted are the standard errors (also called the standard deviation of the means) $\sigma_m = \sigma / \sqrt{N}$, unless otherwise noted. Here N is the number of data points and equals 850 and 170 for the two-layer models and three-layer models, respectively, while σ is the standard deviation of the sample.

This measure of uncertainty is to be distinguished from the confidence interval, which was also calculated. The confidence interval is related to the standard error by the expression $z\sigma_m$, where z depends on α , the significance level. z is the number of standard deviations from the average that includes $(1-\alpha)$ of the area of the normal distribution. In the case of $\alpha=0.05$ (95% confidence), $z=1.96$ (Brown, 1975). Therefore, for an average value μ , the true average would lie between $\mu \pm 1.96\sigma_m$ with 95% confidence. If this

uncertainty in the slope is less than the value of the slope then, with 95% confidence, the slope is distinct from zero.

An equivalent test to determine whether the slopes are distinct from zero, is the t-test. The t-value is calculated, $t = \mu / \sigma_m$. Here μ is the slope determined from linear regression and σ_m is the standard error of the slope. The value of μ distinct from zero when $t > t_{\text{critical}}$, where t_{critical} depends on the number of data points and the significance level, α . This is the same as rejecting the null hypothesis that the slope equals zero. From standard tables, $t_{\text{critical}} = 1.98$ for $N=120$ and approaches 1.96 as N approaches infinity (Beals, 1972). The confidence interval and the t-test yield essentially identical results.

Another method of determining the significance of the slope is the R^2 value, also called the coefficient of determination. The total sum of the squares is equal to the sum of squares due to regression plus the sum of squares due to error. This can be written

$$\Sigma(Y_i - Y_{\text{ave}})^2 = b \Sigma[(X_i - X_{\text{ave}})(Y_i - Y_{\text{ave}})] + \Sigma e_i^2 \quad (3.1)$$

Here b is the slope from the linear regression analysis and e_i is the deviation of the observed values from those estimated from linear regression. If X and Y are totally unrelated then $b=0$, and all of the variation of Y is unexplained. If Y is exactly linearly related to X then all of the e_i 's will be zero and the variation of Y is described by X . The value of R^2 , is the fraction of the variation in the values that is explained by the independent variable (the CMP value).

It is given by,

$$R^2 = b \frac{\sum (X_i - X_{ave})(Y_i - Y_{ave})}{\sum (Y_i - Y_{ave})^2} = 1 - \frac{\sum e_i^2}{\sum (Y_i - Y_{ave})^2} \quad (3.2)$$

and is equal to the ratio of the variation in Y that can be explained by the variation in X, therefore it varies from 0 to 1 (Beals, 1972). As such, R^2 is a measure of the correlation of the independent (X) and dependent variables (Y). The value of R^2 is independent of the scaling of the variables and, therefore, the value R^2 for the velocity is the same as the value R^2 for the concentration data. A t-test on the R^2 value can be used to determine whether a significant correlation exists. In this case, the value for

$t = \sqrt{R^2(N-2)/(1-R^2)}$, which must be greater than $t_{critical}$ for the value of R^2 to be significant (statistically distinct from zero) (Beals, 1972).

All three of the tests give essentially identical results. The values of the slopes are presented for comparison and are not meant to imply that a linear dependence is expected.

B. Layer Thickness

From these model calculations, we observe the thickness of the HSZ increases with distance from the crest of the ridge, independent of the model chosen. For the three-layer models the HSZ minus the constant-velocity sediment layer will be referred to as HSZ'. In all models, the short wavelength variation in the HSZ thickness, as a function of CMP, is much more pronounced than that of the seafloor. Figure 3.1a gives a

representative HSZ' thickness profile as calculated in the three-layer slowness-gradient model. The good reflectors near the BSR, which is what we are actually observing, become faint after CMP ~30000, which makes tracking them and picking traveltime-offset pairs, from trace to trace, quite difficult (see Figure 1.3). This is the source of some of the short-wave variations in our calculation of the thickness of the HSZ.

In the two-layer models, these good reflectors near the BSR are calculated to be approximately a constant distance below the seafloor along Line R22. This is consistent with the interpretation that the BSR is the boundary of the free methane gas and should occur at a roughly constant depth beneath the seafloor (Shipley et al,1979; Sloan,1990). The least-squares trendline shows the thickness is almost constant for the HSZ layer, increasing slightly with distance from the crest of the ridge. The average thickness is 0.49km, with a slope of approximately $4 \pm 0.5 \cdot 10^{-6}$ kilometers/CMP $\approx 7 \pm 0.75 \cdot 10^{-4}$ (km change in thickness)/(km along line), with $R^2=0.1$. (See Table 3.1 for a more detailed compilation of results.) The trendline varies by less than 30 meters over the full 44-km length of the line; less than 6% of the HSZ thickness.

The overlying sediment layer, in the three-layer models, is a relatively thin layer, averaging about 0.03 km (see Table 3.2 for detailed results), that decreases in thickness with increasing distance away from the crest of the ridge (Figure 1b). The inclusion of the sediment layer in the three-layer model results in a thinner HSZ', whose thickness increases with CMP at a faster rate than the two-layer models. The change in thickness with CMP is roughly twice that found in the two-layer model (Table 3.2). Nevertheless, the average depths of the reflectors near the BSR compare quite closely in the two- and three-layer isotropic models 0.49 ± 0.03 and 0.486 ± 0.07 , respectively.

In the anisotropic models, the top two layers are identical to that of the three-layer gradient model while there is an increase in the thickness of the HSZ' layer calculated in the three-layer gradient model. The increase can be more easily identified in Table 3.2. The average thickness increases from 0.457 ± 0.03 km in the isotropic model to 0.480 ± 0.03 km in the three-layer anisotropic constant-velocity model. This indicates that our model of anisotropy yields an increased layer thickness. The slope of the HSZ' thickness with distance from the ridge crest is positive with statistically the same value as in the three-layer model without anisotropy.

C. Layer Velocities

The acoustic velocity of the seawater was set to a constant value for all of the CMP's. The seawater layer was determined separately in the two- and three-layer models because the CMP interval used was different in the two models. The calculated velocities were $1.5094 \pm 4 \cdot 10^{-4}$ km/s (two-layer) and $1.5111 \pm 6 \cdot 10^{-4}$ km/s (three-layer model). These constant isotropic values were used in the calculation of the model values.

The seismic velocity in the uppermost sediment layer was set to a constant throughout the line with a value equal to the average for all of the CMP's. This was done in accord with the understanding that the sediments throughout the ridge are uniform (Paull, 1996). The calculations gave a value of 1.5354 km/s with a standard deviation of $\sigma = 1 \cdot 10^{-3}$. The larger uncertainty is a result of the thinness of the sediment layer.

The seismic velocities that are calculated in the HSZ include the effect of transverse isotropy because of the horizontal layering. Holbrook(2001) has stated that the appropriate velocity to use in the estimation of the concentration of hydrate is the

"equivalent isotropic velocity" which lies between the isotropic and anisotropic values. Since these differ by approximately 5%, we report seismic velocity values that are reduced by 2.5% from our calculations. In the case of the anisotropic models where a 1% anisotropy was used, the velocities were reduced by 3.5%.

The seismic velocities calculated for the HSZ were analyzed through two methods. The Full Line Analysis (FLA) examines Line R22 as a whole and determines whether any overall trends can be discerned. The Partial Line Analysis (PLA) takes advantage of the bright, uniform BSR in the vicinity of the crest where the resulting velocity values have fewer short wavelength variations. Those velocities are fit separately from the remainder of the line. Results from both methods will be presented. Figure 3.2 compares the two methods for the three-layer slowness gradient model. The difference between the two methods of analysis has implications for the question of lateral methane flux.

The seismic velocities in the HSZ in two-layer constant velocity model determined in the FLA, show no systematic dependence on the position along the line. The velocities for the two-layer constant-velocity model are shown in Figure 3.3. This figure indicates that the velocities remain nearly constant along Line R22 throughout the HSZ, with an average value 1.696 ± 0.02 km/s. The slope of the least-squares trendline is given by $-2.68 \pm 3.5 \times 10^{-7}$ km/s/CMP = $-4.28 \pm 5.7 \times 10^{-5}$ (km/s)/km with $R^2=0.0007$. Therefore the small negative slope with increasing CMP, is statistically indistinguishable from a constant velocity throughout the line.

The two-layer slowness gradient model and the constant velocity model are consistent in their description of the velocity profile along the line, using FLA. Unlike

the slight negative trend seen in the constant velocity model there is significant negative trend in the gradient model. The slope of the least squares trendline is $-3.01 \pm 0.66 * 10^{-6}$ km/s/CMP, with $R^2=0.02$. The velocity in the gradient model at 0.460 km beneath the seafloor ($v=1.890 \pm 0.04$ km/s) is greater than the velocity in the constant velocity model ($v=1.696 \pm 0.02$ km/s). The average of the velocity at the top of the HSZ' (1.51 km/s) and at the bottom of the HSZ' equals 1.700 km/s, which is in agreement with the constant velocity model.

Analysis of the two-layer models using the PLA produces somewhat different results. The line was divided into two segments at CMP 29700. The segment below CMP 29700 had a distinctly decreasing velocity characterized by the least-squares fit $-7.66 \pm 1.12 * 10^{-6}$ km/s/CMP (constant velocity) and $-6.96 \pm 2.14 * 10^{-6}$ km/s/CMP (slowness gradient). These slopes are both statistically distinct from zero, showing a decrease in velocity with increasing CMP. The average velocities in the two models were in agreement (1.89km/s (FLA) and 1.90km/s (PLA)). The remainder of the line was found to have a negligible slope, consistent with zero, and a statistically equivalent average velocity. The rms residual, the difference between the "best picks" and the two-layer constant-velocity model travelttime curve, is displayed in Figure 3.4a for the range of CMP's.

The velocity profile in the HSZ', for the three-layer gradient model in the FLA shows only a slight trend with CMP. Figure 3.2 shows the velocity at 0.460 km below the seafloor, with an average value over the CMP's of 1.836 ± 0.03 km/s. The slope of the least-squares trendline is $-6.12 \pm 1.22 * 10^{-6}$ km/s/CMP with $R^2= 0.13$. While this

slope is statistically distinct from zero (at the 95% confidence level), it only amounts to ~0.04 km/s decrease over the 44-km length of the line.

The PLA yields approximately the same average velocity for the three-layer gradient model as the FLA, however the slope is much greater in magnitude. The first segment, to CMP 29700, has a slope of $-1.53 \pm 0.47 * 10^{-5}$ km/s/CMP ($R^2=0.25$) and an average of 1.858 ± 0.01 km/s. The segment above CMP 29700 has a slope that is statistically equivalent to zero and an average velocity of 1.831 ± 0.03 km/s. The velocity decreases as distance from the crest increases in the first segment. The rms residual, the difference between the "best picks" and the three-layer slowness-gradient model traveltimes curve, is displayed in Figure 3.4b for the range of CMP's. These values average about 25% smaller than those for the two-layer constant-velocity model.

The velocity profile for the three-layer anisotropic constant-velocity model was consistent with the three-layer gradient model (Table 3.2). The FLA yields an average velocity of $1.763 \pm .04$ km/s and a negative slope of $-1.76 \pm 1.1 * 10^{-6}$ (km/s)/CMP, with $R^2=0.015$. This negative slope is statistically equivalent to a slope of zero.

The velocity profile for the gradient model with anisotropy, in the FLA, indicates that the velocity is independent of position along the line (Table 3.2). The velocity value at 0.460 km below the seafloor in this model is $1.973 \pm .04$ km/s with a negative slope of $-6.51 \pm 1.74 * 10^{-6}$ (km/s)/CMP, with $R^2=0.08$. The slope is small but distinct from zero.

In the anisotropic models, the PLA cut-off must be placed at higher CMP values in order to have a slope which is substantially different from zero. For a CMP cut-off of 31000, the resulting slopes are $-6.56 \pm 2.4 * 10^{-6}$ km/s/CMP (constant velocity) and

$-2.74 \pm 0.45 \cdot 10^{-5}$ km/s/CMP (gradient). Both of these slopes are statistically significant, indicating that over this range the velocity decreases. The average values of velocity in each segment are equivalent to those of the FLA. This cut-off was also used for the isotropic models and produced decreasing velocities in those cases as well.

We conclude from these models that within the FLA the velocity changes very slowly with distance from the crest of the ridge, being statistically distinct from zero only in the three-layer slowness linear-gradient model. Velocities for the isotropic models are in reasonable agreement with each other, while the anisotropic models have slightly higher values with larger uncertainties. When Line R22 is broken into segments, the PLA shows that there is a decreasing velocity in the immediate region of the crest with increasing CMP.

D. Concentration

We estimate methane hydrate concentrations from seismic velocities using the formulation of Helgerud (2001). Helgerud (2001) uses a theoretical rock physics model to relate the elastic properties of the sediment to the porosity, mineralogy, and effective pressure, with the contribution of fluid to the effective elasticity of the media determined from Gassmann's equations. The porosity was taken from shipboard core measurements (at site 995), while the effective pressure was calculated as the difference between the overburden and hydrostatic pressure. The composition was measured to be 60% clay, 35% calcite, and 5% quartz, with a coordination number of nine and a critical porosity of 37% (the porosity above which all grains are disconnected) (Helgerud, 2001). Helgerud (2001) calculates constant-concentration velocity versus depth profiles. These profiles

which are based on site 995 have to be extended beyond this site for seismic data to be interpreted.

Several assumptions and approximations are necessary to use the site 995 models over the length of the line. The sediments throughout the Blake Ridge are uniform (Paul et al., 1996), so seismic variations can be interpreted to be variations in hydrate concentrations (Holbrook et al., 1996). Therefore, we assume that a single "universal" zero-concentration velocity versus depth profile can be used along the full line. One set of techniques to arrive at this profile is to use a generalized porosity, ϕ , as a function of depth. Davies and Buffet (2001) proposed $\phi(z) = \phi_0 \exp(-z/L)$ where z is the depth and L is the compaction length scale (~2 km). Using this formulation the profile can be calculated using the first-principle physics method of Helgerud or the empirical weighted-average equation of Lee (Lee et al., 1996).

The weighted-average equation determines the compressional velocities in the layer from the porosity, hydrate concentration, compressional velocities of hydrate bearing sediments, and a constant simulating the rate of lithification with hydrate concentration (Lee et al., 1996). The weighting factor determines the relative contribution of two model compressional velocities (Lee et al., 1996). Work by Lee and Collett (2001), show that p-wave velocities calculated using both the weighted-average equation and Helgerud's effective-medium equation (2001) are in close agreement but differ for shear waves.

Rather than fitting the porosity to smooth out the local anomalies and then calculating the profile using Lee's weighted-average equation (Lee et al., 1996), we decided to smooth the zero-concentration profile of Helgerud (2001) directly, which

should give comparable results (Collett and Lee, 2001). This decision was made because of the wide-spread use of Helgerud's method and results in the Blake Ridge region.

The zero concentration profile found by Helgerud (2001) at site 995 has local porosity variations, which are not expected at other sites. To get the "universal" profile, Helgerud's profile is fit to smoother functions to eliminate the variations. We find that linear, quadratic and logarithmic functions describing velocity versus depth give good fits ($R^2 > .95$). Concentrations estimated by Helgerud's profile, or any of the other functional forms, give reasonably similar concentrations with depth, within about 1% hydrate concentration, and average concentration values that are nearly identical. This consistency reinforces our decision to model Helgerud's profile since the concentrations are not sensitive to fluctuations in the profile. We choose the simplest least-squares trendline:

$$v_0 = .4351 * z + 1.534 \quad (3.3)$$

This eliminates the anomalies associated with localized variations in porosity and has the coincidental result that the $z=0$ velocity is almost identical to the velocity in the sediment layer (see Table 3.2). Along with seismic velocities, this profile is then used to determine concentrations along the length of line R22 (Figure 3.5).

While the velocity for 0% concentration varies with depth because of porosity, mineralogy, and effective pressure, the change of velocity with concentration $\frac{dv}{dc}$ is nearly constant for concentrations up to 30% and independent of depth (Helgerud, 2001;

Hornbach et al., 2003). Therefore, in our work, the value $\frac{dv}{dc}$ is approximated by a constant. The linear relation used for the hydrate in the pore was $c(\%) = (v - v_0) * 100$. Nevertheless, $\frac{dv}{dc}$ does depend on whether the methane hydrate is suspended in the pore fluid or is a load-bearing component of the sediment frame. From Helgerud's results (2001), the relation between the two derivatives is found to be $1.4 \frac{dv}{dc} |_{\text{pore}} \approx \frac{dv}{dc} |_{\text{frame}}$. These two descriptions are expected to be limiting values. The velocity at the top of the HSZ, assumed to have a methane hydrate concentration nearly equal to 0%, is taken in this work to be 1.6km/s.

Three different cases were considered:

a) The constant velocity model (2 layers):

Since the velocity is constant throughout the HSZ, the center of the layer (0.230km below seafloor) is the depth used to determine the concentration dependence on velocity.

b) A gradient velocity (near bottom of HSZ):

In this case the depth used to determine the concentration dependence on the velocity is the constant depth of 0.460 km below the seafloor approximating the depth of the BSR. Since the velocity at this depth is the highest this yields the largest concentration.

c) A gradient velocity (middle of the HSZ):

In this case a depth of 0.230 km below the seafloor is used to determine the velocity used for the concentration calculation.

Because of the uncertainties entailed, concentrations are rounded to $\frac{1}{2}\%$.

The two-layer constant velocity model gives the lowest concentration values. The concentration found in the frame model (4.5%) is less than in the pore model (6%) (See Table 3.1). Both concentrations have slopes with CMP which are consistent with the velocity slopes in the FLA and negative near the crest in the PLA. In the PLA the slopes are given by $-7.66 \pm 1.1 \cdot 10^{-4} \%$ /CMP and $-5.47 \pm 0.78 \cdot 10^{-4}$ in the pore and frame, respectively. This is equivalent to an approximately 1% decrease in concentration in this segment.

In the two-layer slowness-gradient model, the concentration values are larger than found in the constant velocity model. The concentration at 0.230km below the seafloor in the frame model (4.5%) is less than the value at 0.460 km(11.5%). In the PLA, the slope decreases with CMP near the crest ($4.97 \cdot 10^{-4} \%$ /CMP) and in the FLA it decreases with slope $2.10 \cdot 10^{-4} \%$ /CMP. This amounts to a 1.5% change in the concentration over the length of the line.

The concentrations obtained in the three-layer slowness-gradient model decrease with distance from the ridge. For all of the concentrations the slopes are all very slightly negative and distinct from zero with 95% confidence. For example, the concentration of methane hydrate, at 0.460km, when it is modeled as part of the frame, is $7.5 \pm 2\%$ with a slope of $-4.4 \pm .9 \cdot 10^{-4} \%$ /CMP. This can be compared with the PLA where a value of $-1.09 \cdot 10^{-3} \%$ /CMP is calculated, corresponding to a decrease in concentration of approximately 2% in the segment (Fig. 3.6).

The average concentration for the methane hydrate, determined as part of the frame in the three-layer slowness-gradient model, ranges from 3% to 7.5% as the depth

goes from 0.230km to 0.460 km beneath the seafloor, roughly the middle of the HSZ to the bottom. The three-layer anisotropic constant-velocity model estimates concentration of $9\% \pm 2\%$, which corresponds roughly to a value in the middle of the HSZ'.

In the three-layer anisotropic slowness-gradient model the concentration values show the same trends that were witnessed before. Their derivation requires that they mirror the velocity trends and, as a result, show only a slight statistical dependence on position in the FLA. In the PLA, the concentration dependence on position near the crest is given by $-2.74 \pm 0.45 \cdot 10^{-3} \text{ %/CMP}$. For this segment the decrease in concentration is approximately 4%. The three-layer anisotropic slowness-gradient model produces the largest concentrations (Table 3.2).

The change of concentration with depth is estimated by using the linear constant-concentration profiles described above. In Figure 3.7, the concentration as a function of depth is plotted for several selected CMP's. The increase of concentration with depth is evident. Figure 3.8 shows how the concentrations for the selected CMP's vary from the concentration averaged over all of the CMP's.

E. Table Captions

Table 3.1: Results for Two-Layer Models

Results for two-layer constant velocity and slowness-gradient models are given. The slopes are determined from least-square fits to the data. Uncertainties listed are one standard error. The uncertainties for average values, as opposed to slopes, are calculated with respect to the appropriate least-squares trendline (also referred to as the standard error in "y"). Concentrations and their uncertainties are only given to the nearest one-half percent. Abbreviations used for the labels: (pore, 230m) corresponds to the methane hydrate being part of the pore fluid and the concentration is calculated at 230 meters below the sea floor, near the middle of the HSZ; (pore, 460m) is same as above except the concentration is calculated near the bottom of the HSZ; (frame, 230m) corresponds to the methane hydrate being part of the frame structure and the concentration is calculated at 230m below the seafloor; (frame,460m) is same as above except the concentration is calculated at 460m below the seafloor.

Table 3.2: Results for Three-Layer Models

Results for the three-layer slowness-gradient model, the three-layer anisotropic slowness-gradient model, and the three-layer anisotropic constant-velocity model are given. The slopes are determined from least-square fits to the data. Uncertainties listed are one standard deviation. The uncertainties for average values, as opposed to slopes, are calculated with respect to the appropriate least-squares trendline (also referred to as the standard error in "y"). Concentrations and their uncertainties are only given to the nearest one-half percent. Abbreviations used for the labels: (pore, 230m) corresponds to the methane hydrate being part of the pore fluid and the concentration is calculated at 230 meters below the sea floor, near the middle of the HSZ'; (pore, 460m) is same as above except the concentration is calculated near the bottom of the HSZ; (frame, 230m) corresponds to the methane hydrate being part of the frame structure and the concentration is calculated at 230m below the seafloor; (frame,460m) is same as above except the concentration is calculated at 460m below the seafloor.

Table 3.1: Results for Two-Layer Models

	2-layer constant -velocity model	2-layer slowness-gradient model
Velocity Seawater (km/s)	1.509354	1.509354
Velocity top of HSZ (km/s)	1.696 ± .02	1.55
Slope (km/s/CMP)	(-2.68 ± 3.5)*10 ⁻⁷	0
Velocity (km/s) at 460mbsf	1.696 ± .02	1.890 ± 0.04
Slope (km/s/CMP)	(-2.68 ± 3.5)*10 ⁻⁷	(-3.01 ± 0.66)*10 ⁻⁶
Thickness of HSZ (km)	0.491 ± 0.03	0.489 ± 0.025
Slope (km/CMP)	(4.21 ± 0.47)*10 ⁻⁶	(4.33 ± 0.45)*10 ⁻⁶
Concentration (pore, 230m) (%)	6 ± 2	6.5 ± 2
Slope (%/CMP)	(-2.7 ± 3.5)*10 ⁻⁵	(-1.3 ± 0.27)*10 ⁻⁴
Concentration (pore, 460m) (%)	6 ± 2	16 ± 4
Slope (%/CMP)	(-2.7 ± 3.5)*10 ⁻⁵	(-3.01 ± 0.66)*10 ⁻⁴
Concentration (frame, 230m) (%)	4.5 ± 2	4.5 ± 2
Slope (%/CMP)	(-2.1 ± 2.8)*10 ⁻⁵	(-9.3 ± 1.9)*10 ⁻⁵
Concentration (frame, 460m) (%)	4.5 ± 2	11.5 ± 3
Slope (%/CMP)	(-2.1 ± 2.8)*10 ⁻⁵	(-2.1 ± .49)*10 ⁻⁴

Table 3.2: Results for Three-Layer Models

	3-layer gradient model	3-layer gradient w/anisotropy	3-layer constant w/anisotropy
Velocity Seawater (km/s)	1.511142	1.511142	1.511142
Velocity Sediment (km/s)	1.535417	1.535417	1.535417
Velocity top of HSZ' (km/s)	1.6	1.6	1.763 ± 0.03
Slope (km/s/CMP)	0	0	(-1.76 ± 1.1)*10 ⁻⁶
Velocity (km/s) at 460mbsf	1.836 ± 0.04	1.973 ± 0.04	1.763 ± 0.03
Slope (km/s/CMP)	(-6.12 ± 1.22)*10 ⁻⁶	(-6.51 ± 1.74)*10 ⁻⁶	(-1.76 ± 1.1)*10 ⁻⁶
Thickness of Sediment Layer (km)	0.0294 ± 0.004	0.0294 ± 0.004	0.0294 ± 0.004
Slope (km/CMP)	(-5.48 ± .15)*10 ⁻⁶	(-5.48 ± .15)*10 ⁻⁶	(-5.48 ± .15)*10 ⁻⁶
Thickness of HSZ' (km)	0.457 ± 0.03	0.477 ± 0.023	0.48 ± 0.03
Slope (km/CMP)	(8.09 ± 0.9)*10 ⁻⁶	(8.52 ± 0.9)*10 ⁻⁶	(8.11 ± 0.9)*10 ⁻⁶
Concentration (pore, 230m) (%)	4.5 ± 2	8.5 ± 2	11 ± 3
Slope (%/CMP)	(-5.3 ± 4.9)*10 ⁻⁵	(5.0 ± 6.7)*10 ⁻⁵	(-1.76 ± 1.1)*10 ⁻⁴
Concentration (pore, 460m) (%)	10 ± 3	24.5 ± 5	12 ± 3
Slope (%/CMP)	(-6.12 ± 1.22)*10 ⁻⁴	(-6.51 ± 1.74)*10 ⁻⁴	(-1.76 ± 1.1)*10 ⁻⁴
Concentration (frame, 230m) (%)	3 ± 1	6 ± 2	8.5 ± 2
Slope (%/CMP)	(-3.9 ± 3.6)*10 ⁻⁵	(3.6 ± 4.8)*10 ⁻⁵	(-1.2 ± 0.8)*10 ⁻⁴
Concentration (frame, 460m) (%)	7 ± 2	17.5 ± 4	8.5 ± 2
Slope (%/CMP)	(-4.5 ± 0.9)*10 ⁻⁴	(-4.7 ± 1.3)*10 ⁻⁴	(-1.2 ± 0.8)*10 ⁻⁴

F. Chapter 3 Figure Captions

Figure 3.1

Layer structure along line R22 in the Blake Ridge. (a) Thickness of the HSZ' in the three-layer slowness-gradient model (b) Layer structure showing seawater, thin sediment layer and HSZ.

Figure 3.2

Seismic velocity at 0.46 km below the seafloor along Line R22 calculated in the three-layer slowness-gradient model. a) The FLA analysis covering the full length of the line, and b) The PLA analysis with trendlines superimposed showing the greater change of velocity with position near the crest. The trendline in the flank has a slope which is statistically equivalent to zero.

Figure 3.3

Seismic velocity in the HSZ hydrate along Line R22 calculated in the two-layer constant-velocity model. The slope of the trendline is statistically equivalent to zero.

Figure 3.4

The rms difference of the "best picks" from the model traveltime curve for a) the two-layer constant-velocity model and b) the three-layer slowness gradient model.

Figure 3.5

Constant-hydrate concentration profiles as a function of depth. The linear model fit is used for a range of concentrations with the zero concentration of Helgerud (2001) superimposed. The thick black line is the average gradient velocity (over all CMP's) generated from the three-layer slowness-gradient model. a) a model in which the hydrate fills the pore fluid, and b) a model in which the hydrate is part of the frame.

Figure 3.6

Concentration (% volume) of methane hydrate along line R22 in the Blake Ridge. Concentration was estimated using velocities calculated in the three-layer slowness-gradient model and applying linear constant-concentration profiles.

Figure 3.7

Change of concentration with depth for selected CMP's. The concentrations are estimated using the linear constant-concentration profiles. The average value is found from an average over all CMP's.

Figure 3.8

Differences in concentration from the average for selected CMP's.

HSZ Thickness

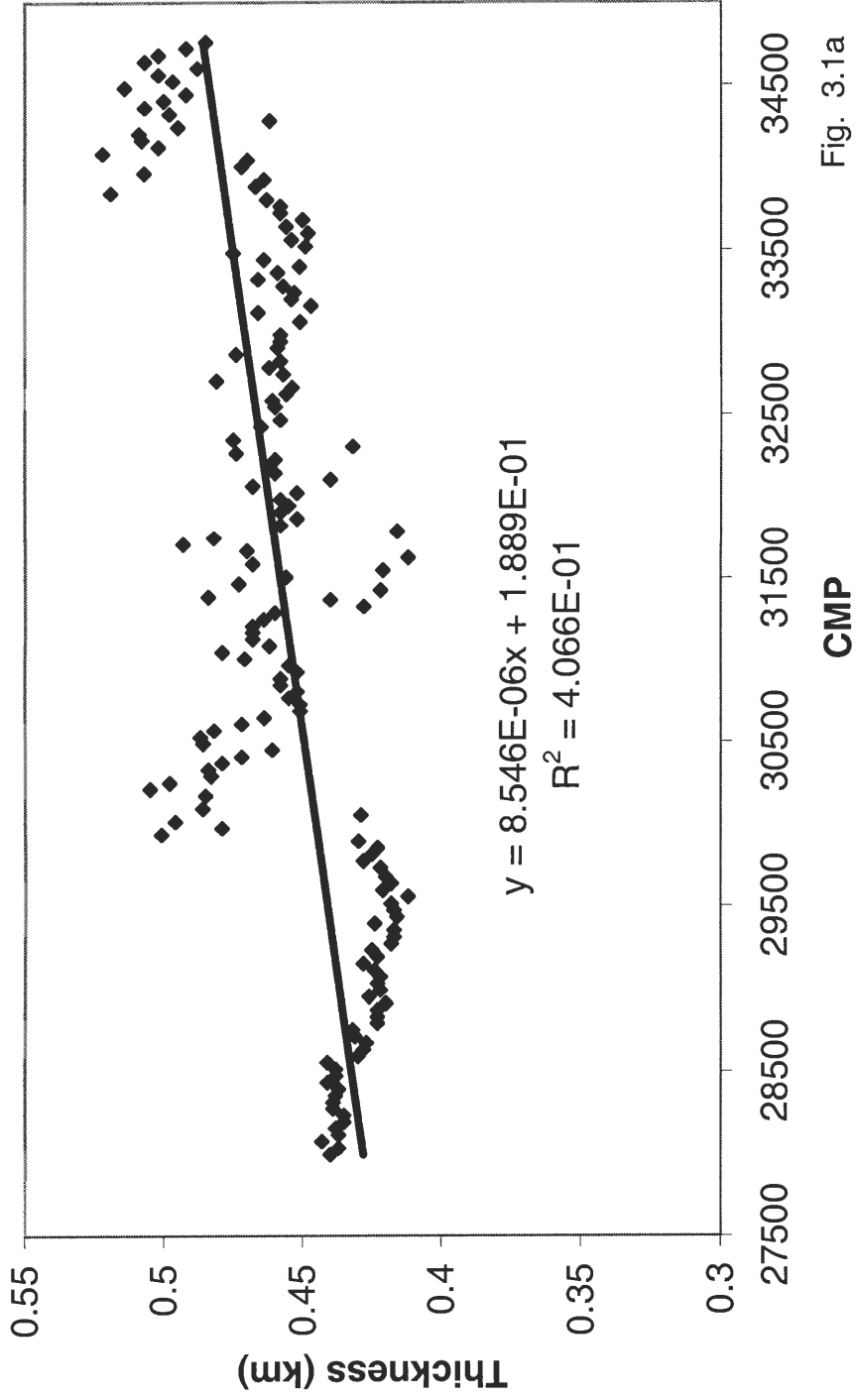


Fig. 3.1a

Layer Structure (3-layer, Slowness-Gradient)

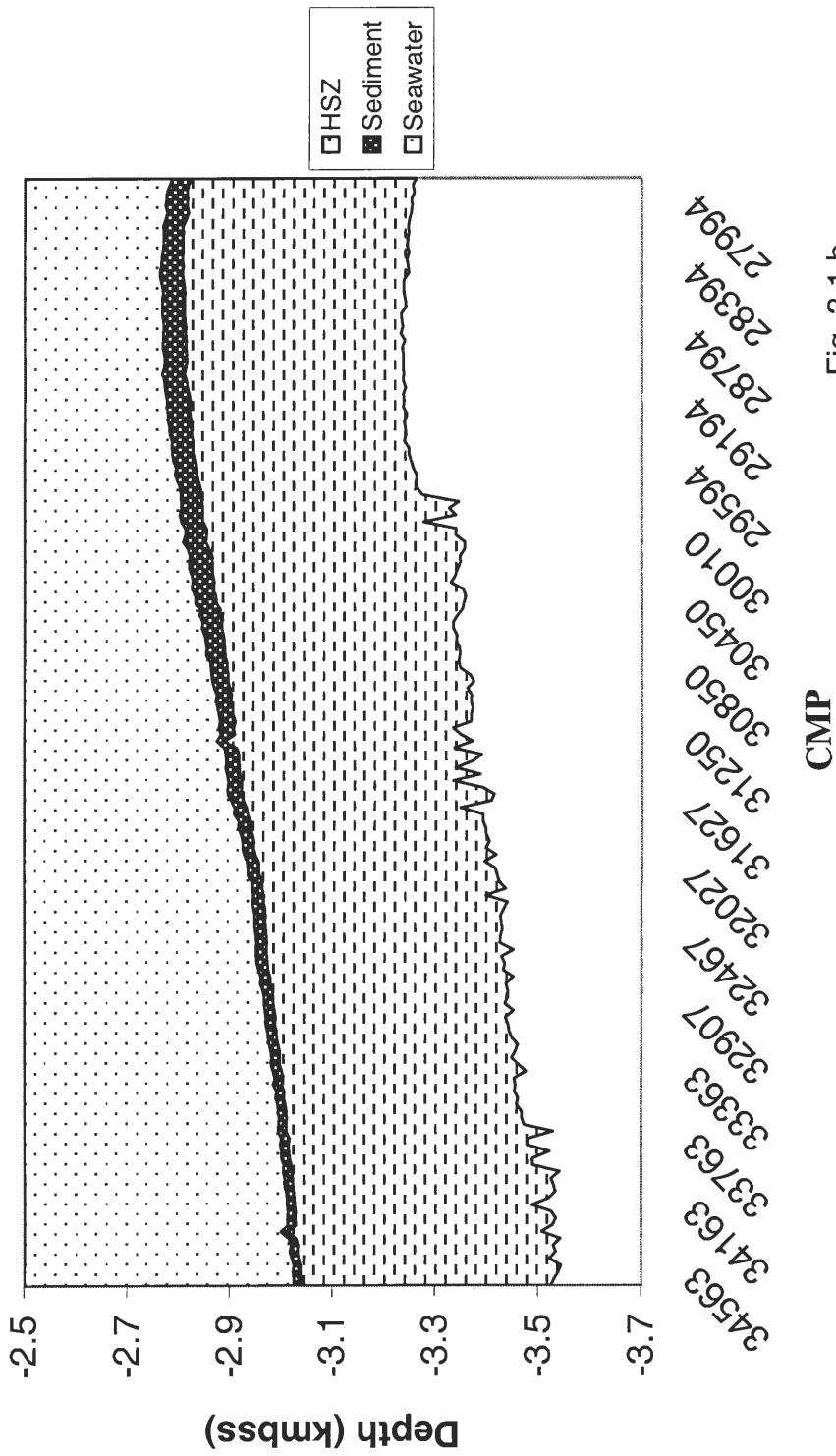


Fig. 3.1.b

3-Layer gradient (Vel at 460mbsf)

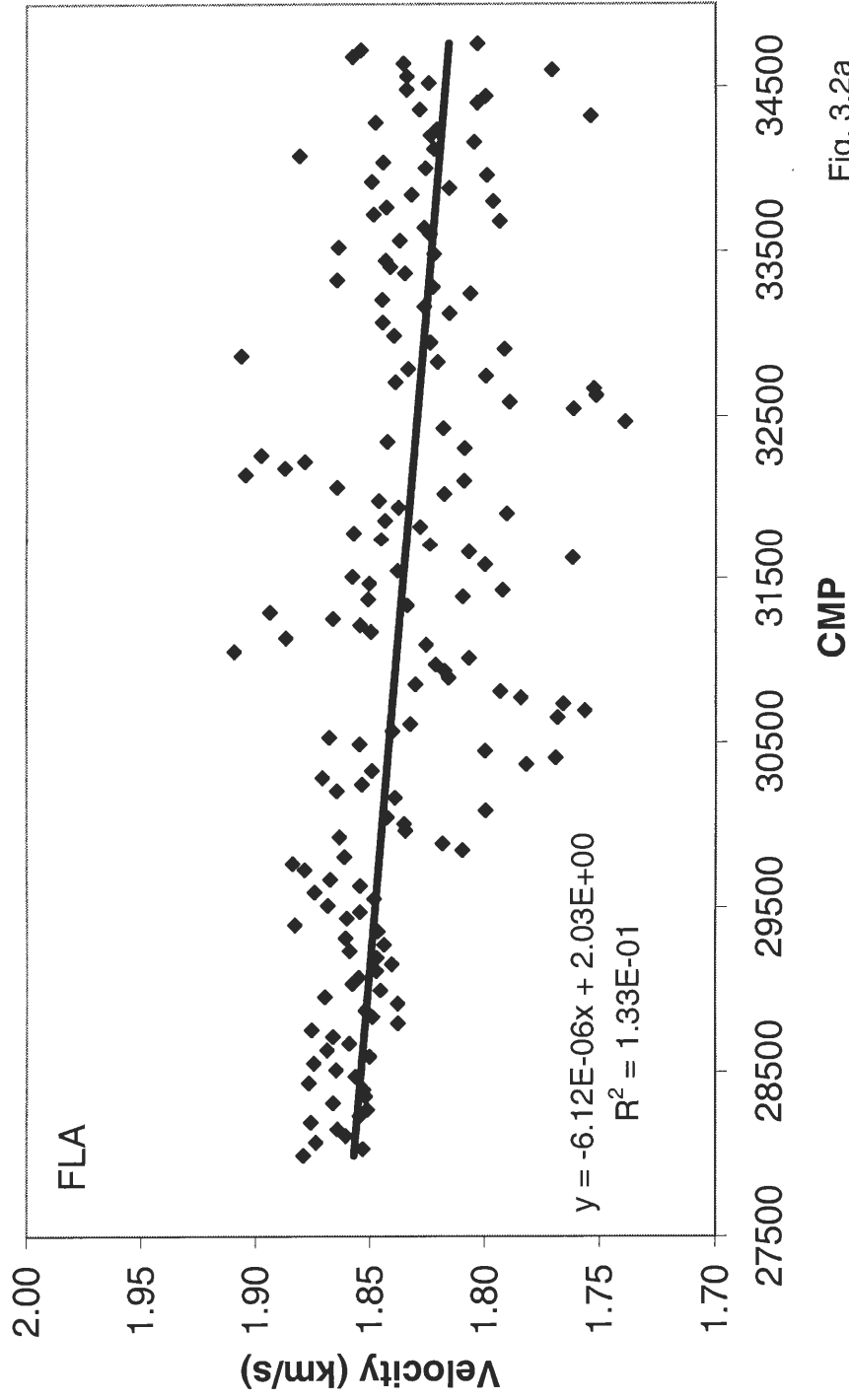


Fig. 3.2a

Velocity at 460 mbsf

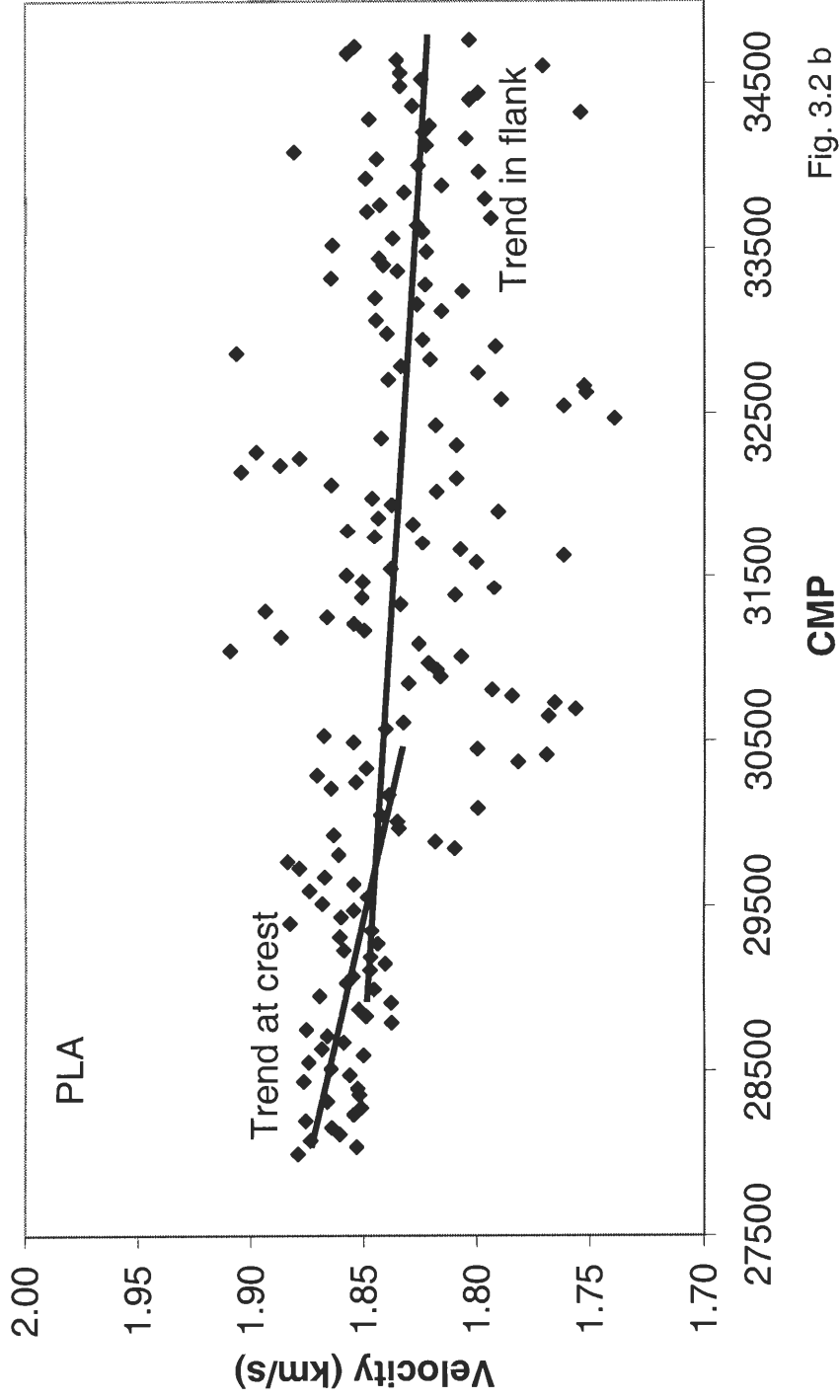


Fig. 3.2 b

Velocity in HSZ

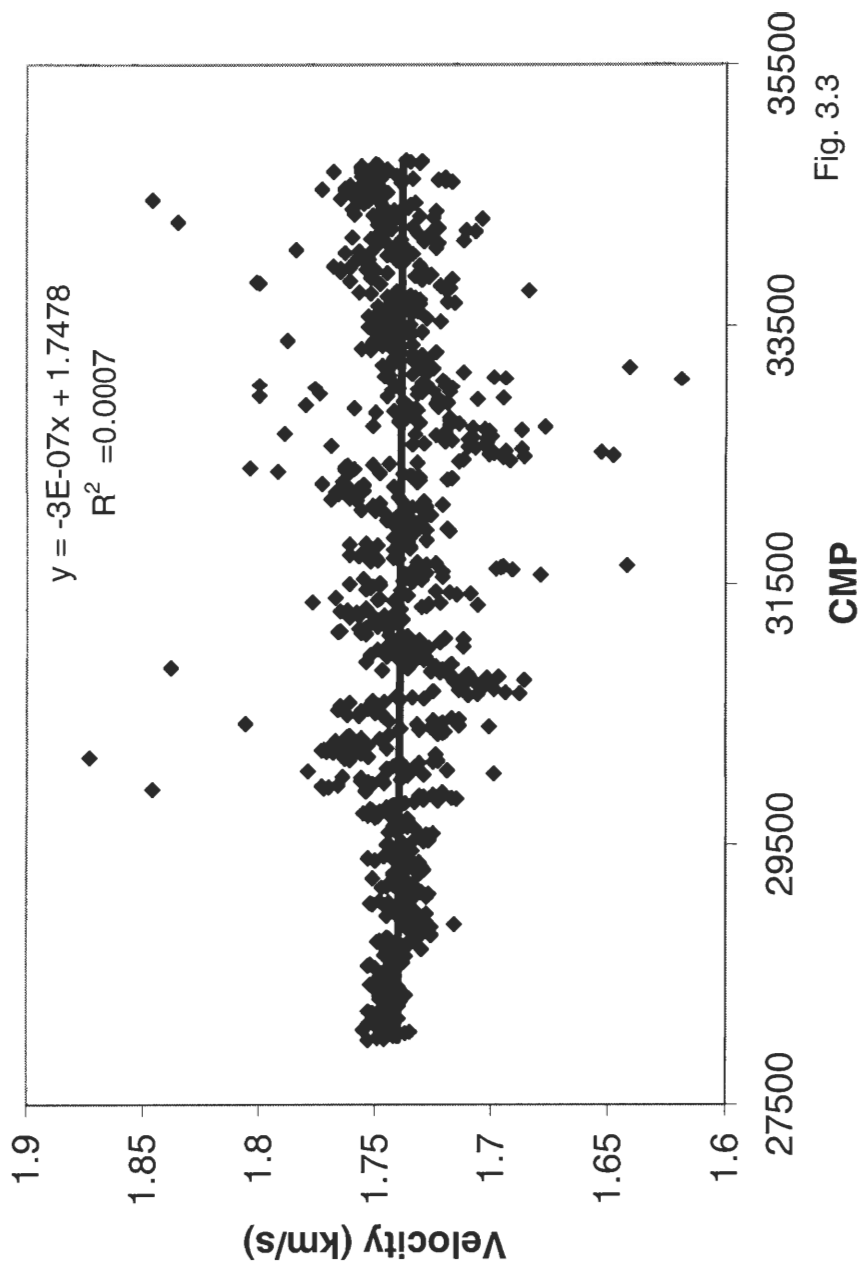


Fig. 3.3

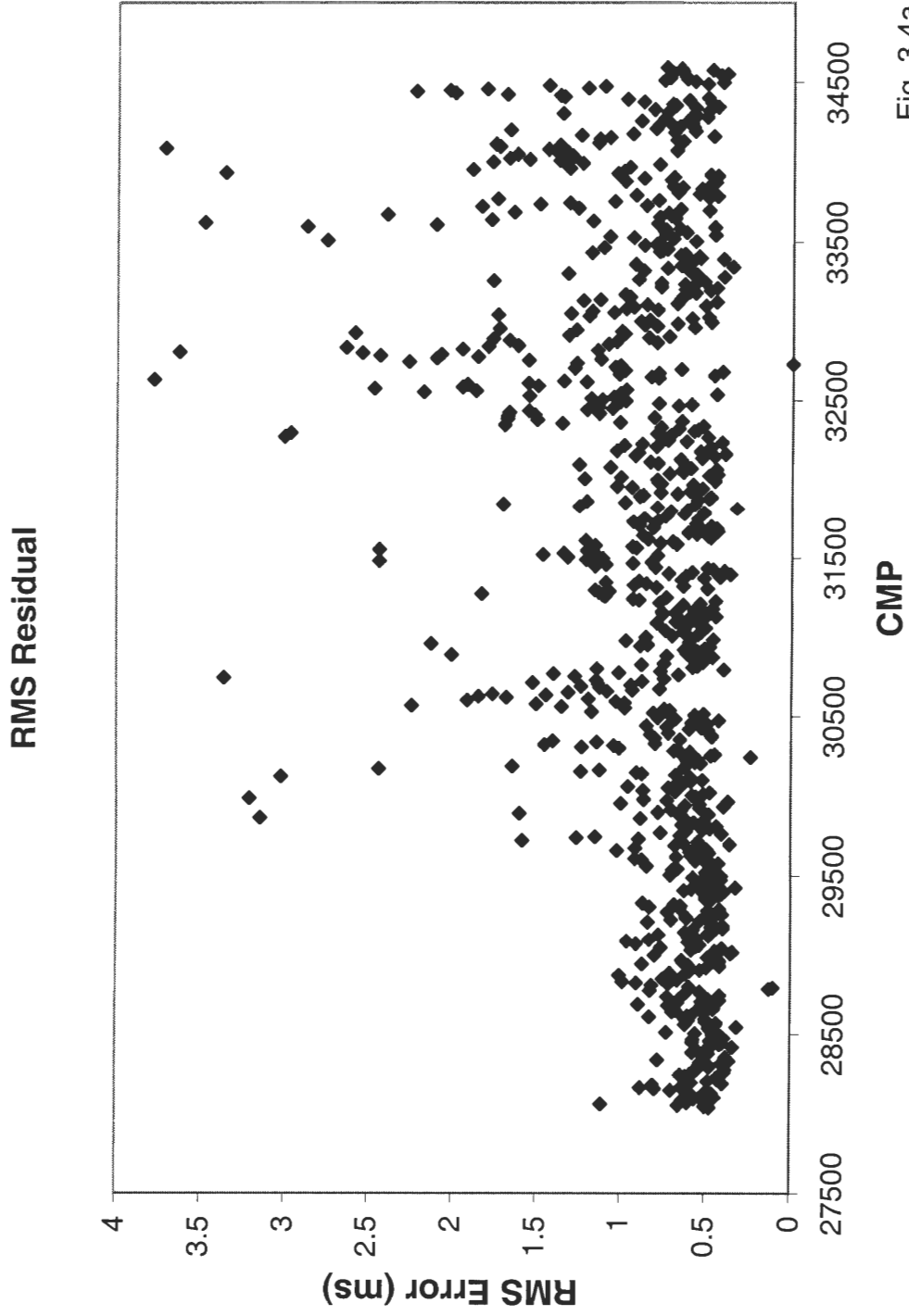


Fig. 3.4a

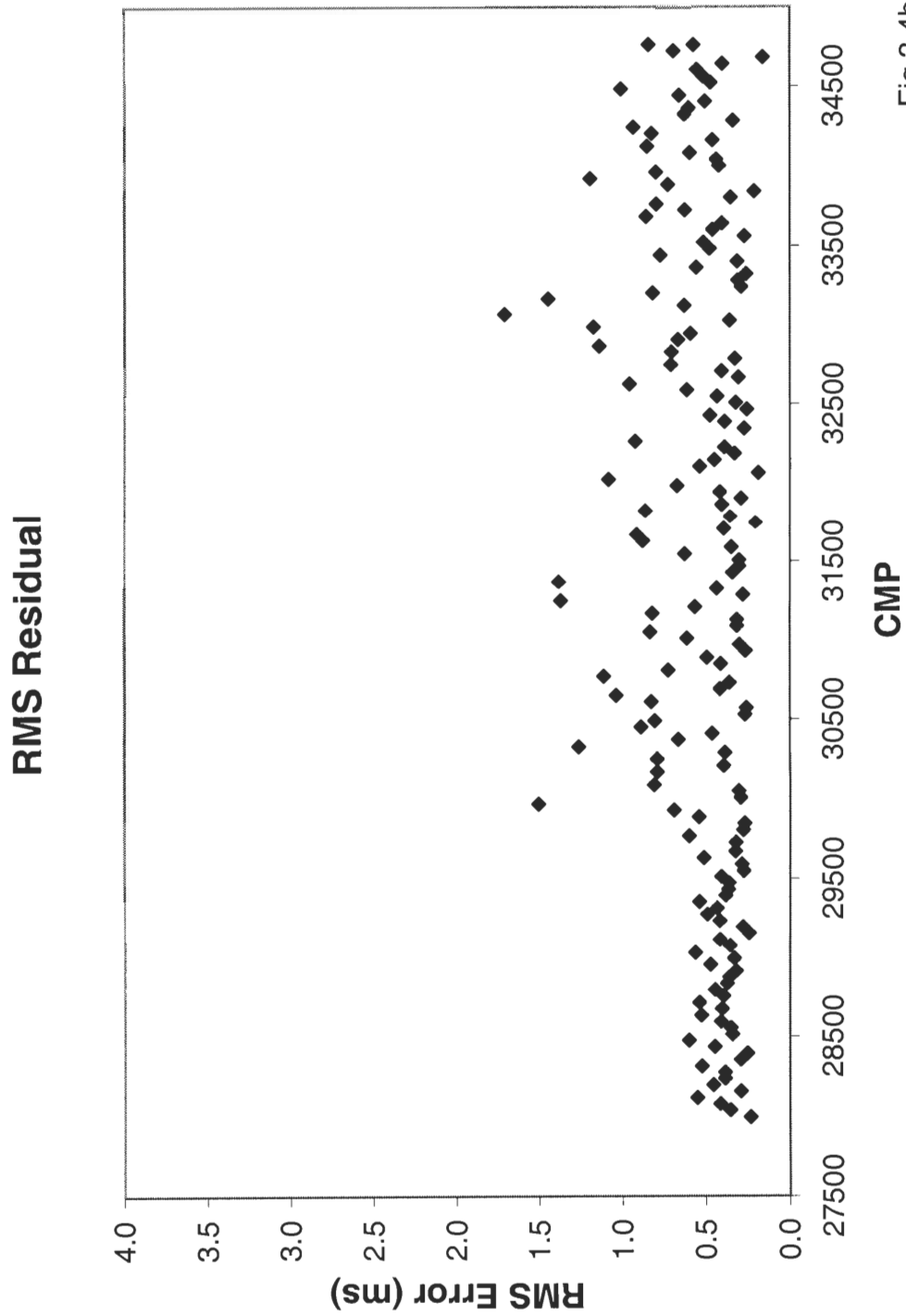


Fig 3.4b

Concentration Profile (Pore)

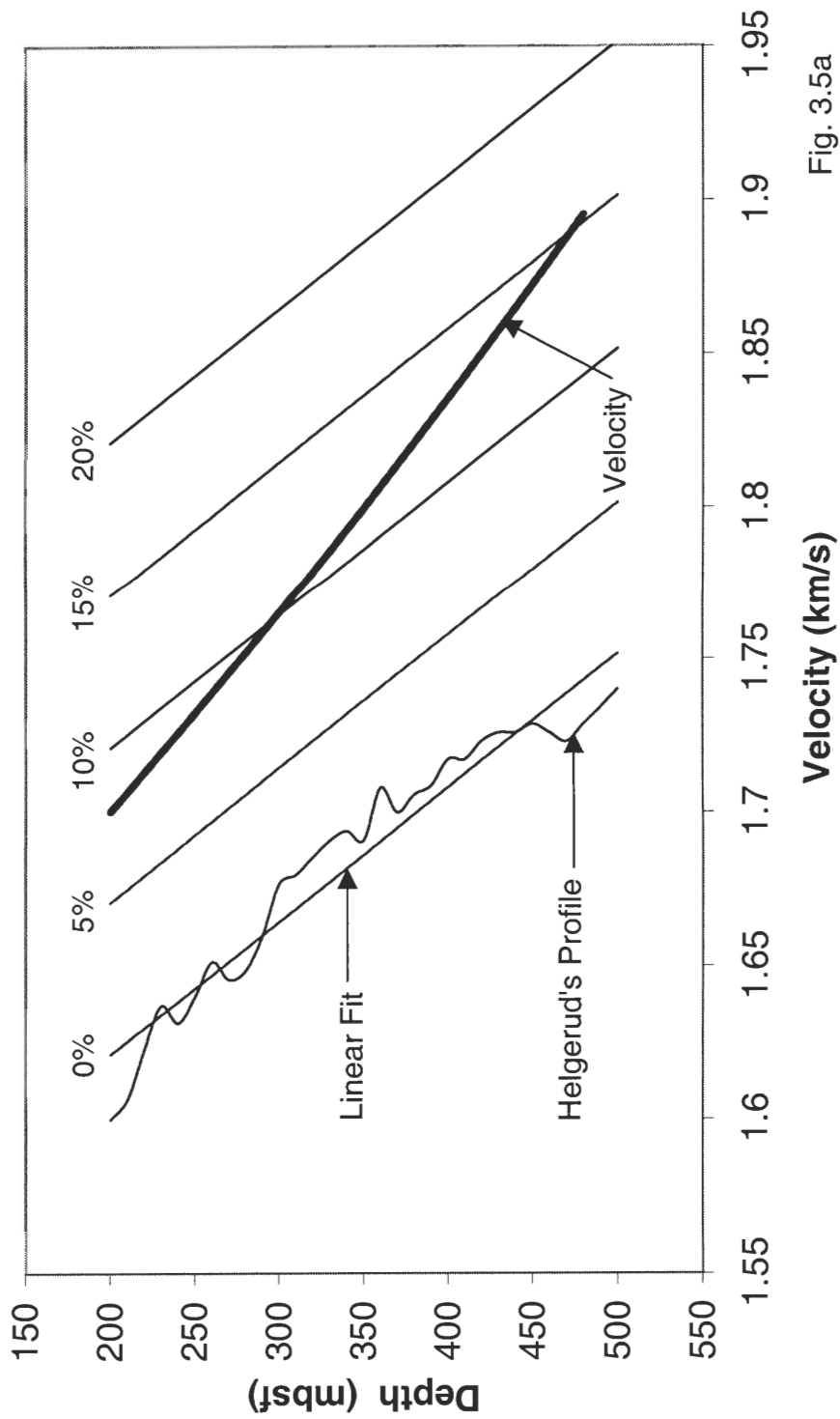


Fig. 3.5a

Concentration profile (frame)

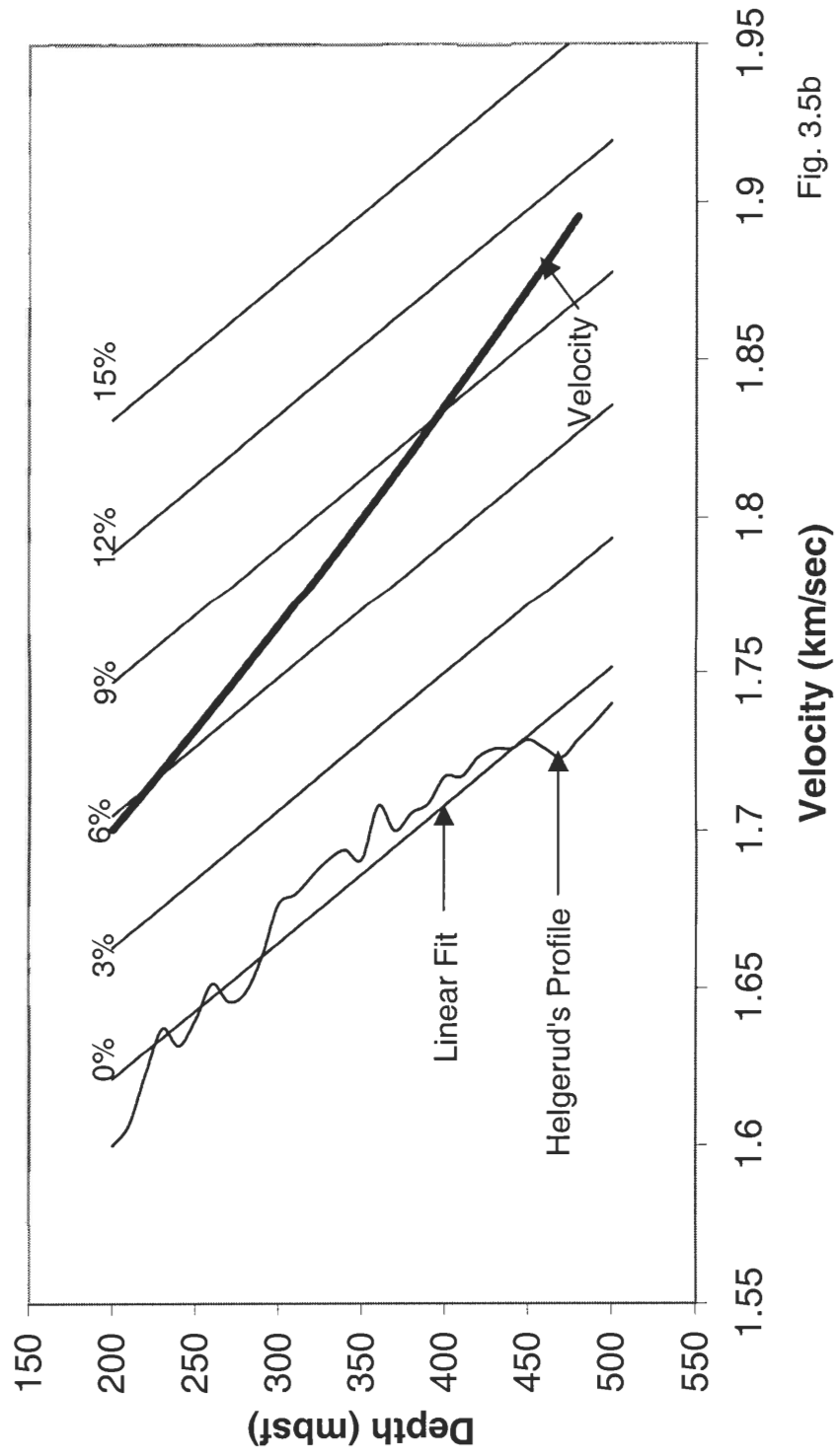


Fig. 3.5b

Concentrations (3-Layer Gradient Model)

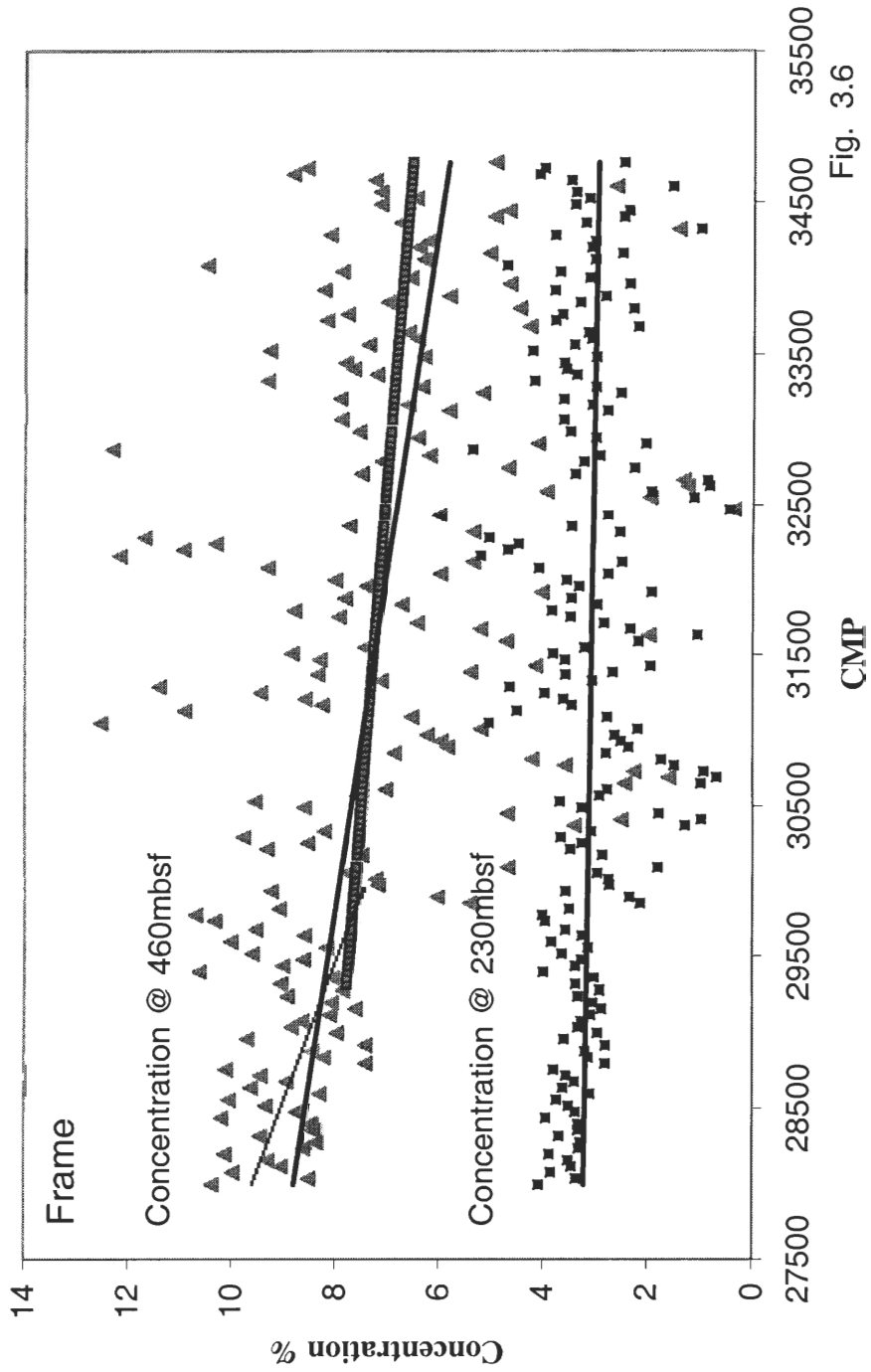


Fig. 3.6

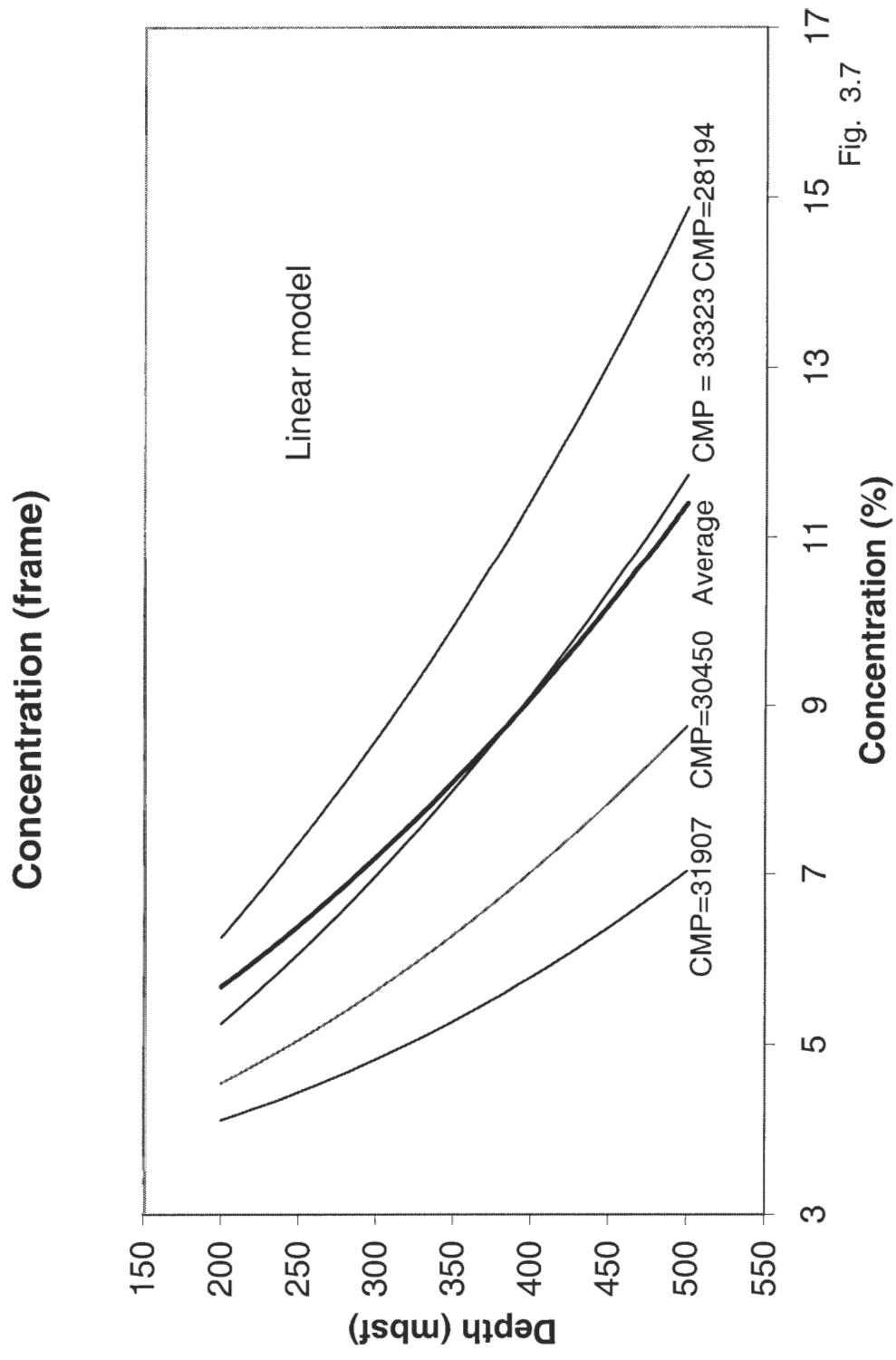


Fig. 3.7

Concentration Differences

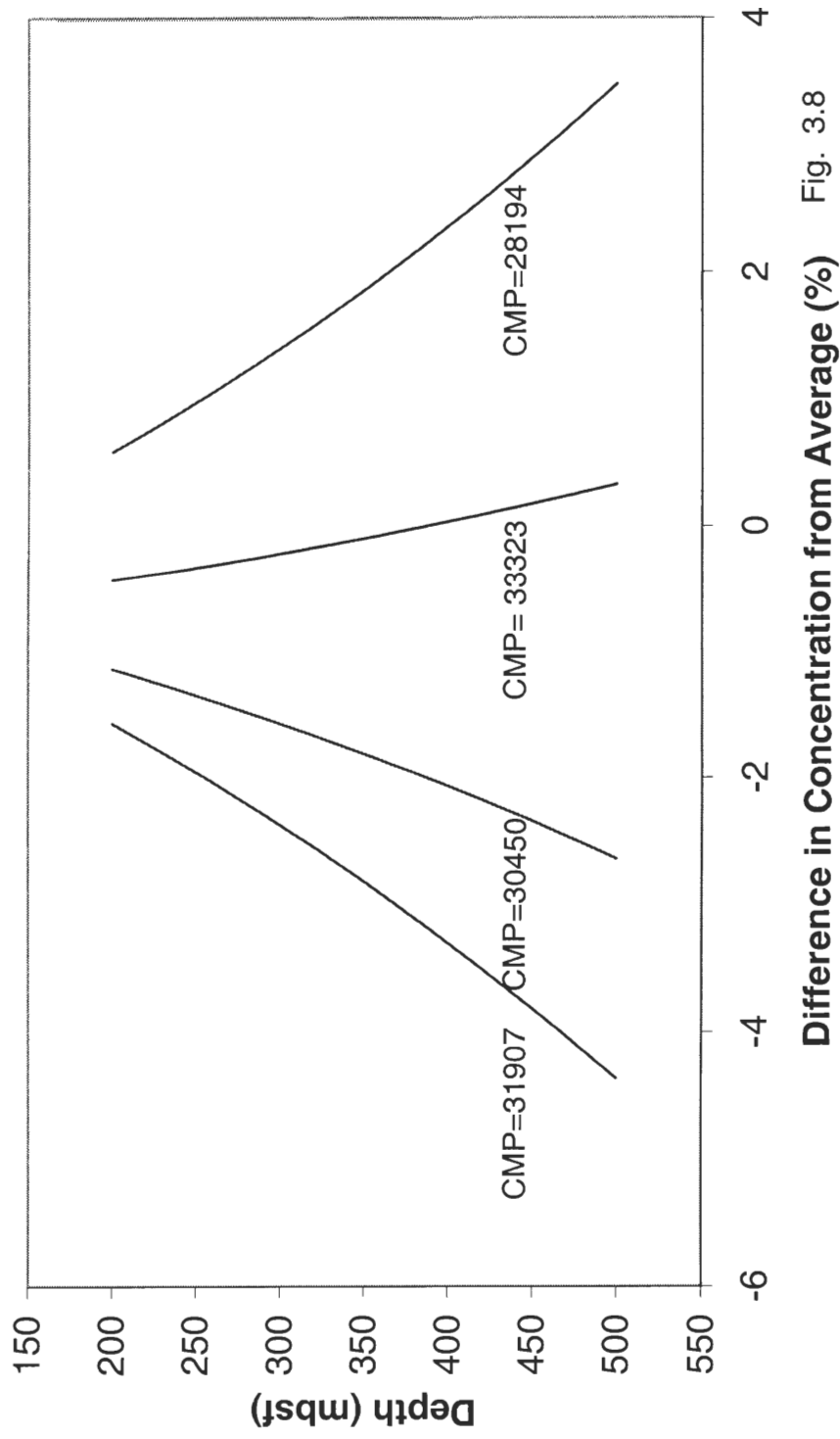


Fig. 3.8

Chapter 4

Discussion

A. Discussion

Based on the MCS reflection traveltimes, the velocity models indicate that the seismic velocity of the HSZ, has a significant dependence on position near the crest of the ridge. From this, we can infer that the related methane hydrate concentration also has a significant dependence. In this region, the velocity decreases with distance in all of the models studied. Over the remainder of the line, there is no significant systematic change in velocity with position. The conclusion that, independent of the model, the concentration shows a position dependent decrease in the vicinity of the crest suggests the presence of two-dimensional transport.

The estimated hydrate concentrations depend upon the velocity model that was used. In the two-layer constant velocity model the average concentration for the entire line is $4.5 \pm 2\%$ (with hydrate as part of the frame), while in the two-layer gradient model the comparable average in the middle of the HSZ, 0.230km below the seafloor, is also $4.5 \pm 2\%$. The three-layer slowness gradient model yields the similar concentration of 3% . The results for these three models are consistent with each other at the 95% confidence level. The values for the hydrate concentrations determined from the anisotropic models are significantly larger with averages of $6 \pm 2\%$ (slowness-gradient model) and $8.5 \pm 2\%$ (constant-velocity model) (Table 3.2).

Concentrations of methane hydrate that have been previously estimated through studies at boreholes, serve as useful references. VSP data taken at boreholes 994, 995 and

997, yielded velocities of 1.75 km/s to 1.85 km/s at 0.45 km below the seafloor (Holbrook et al, 1996). The velocities from 0.20 km to 0.45 km beneath the seafloor were found to be consistent with concentrations of hydrate filling 5% to 7% of the porosity at site 995 and 997 (Holbrook et al.,1996). More recent analysis of site 997 shows a mean velocity of 1.80km/s at 0.40 km below the seafloor (Holbrook, 2001). Holbrook converted this to a hydrate concentration of 4% (hydrate in frame), following the work of Helgerud et al. (1999). These values are in close agreement with the three-layer slowness gradient model, which yields a velocity of 1.836 km/s at 0.46 km below the seafloor and a concentration range of 3% - 10.5% between 0.23 km and 0.46 km beneath the seafloor.

The depth of the BSR below the seafloor, as approximated by finding the depth to the nearest reflector, can also be compared to previous results. The three layer slowness-gradient model yields a depth of 0.474 km in the vicinity of borehole 997. This depth compares with Holbrook (2001) and Paull et al. (1996) at site 997 where p-wave velocities resolved from VSP data indicate a BSR with a depth of 0.44 km below the seafloor.

The pressures at the top of the HSZ and at the BSR are displayed in Figure 4.1, illustrating the increase in pressure with distance from the crest. The calculation includes the varying thickness of the water column, sediment layer, and HSZ, with an average porosity of 0.6. The temperature profile at site 997 (Wood and Ruppel, 2000) and the phase equilibrium curve for seawater (Peltzer and Brewer, 2000) are plotted in Figure 4.2. Their intersection should approximate the base of the HSZ. Superimposed is the range of pressures that were found in Figure 4.1. The overlap of these results suggests

that our calculated depth of the bottom of the HSZ is consistent with the hydrate-free gas phase boundary.

The estimates of hydrate concentration enable inferences to be made regarding whether the flow of methane is predominantly one-dimensional, or if there is a significant lateral flow. Vertical methane flux is thought to be controlled predominately by compaction driven vertical fluid flux in combination with *in situ* methane production (Xu and Ruppel, 1999). Two-dimensional flow depends upon the availability of contrasting permeability pathways, in which methane is trapped or diverged in a direction away from vertical (Gorman, 2002).

If the *in situ* production of methane is uniform as expected (Paull, 1996), the resulting hydrate concentration should also be uniform, unless there is lateral transport of methane in addition to the vertical flux. The FLA indicates that the hydrate concentration exhibits little or no trend with distance from the crest. This is consistent with a dominant vertical flux. The PLA, however, indicates that the region near the crest of the ridge has a significant decreasing concentration of hydrate with distance from the peak. The concentration levels off to an approximately uniform value in the flank. From this estimate of the distribution of hydrate concentration, we infer that lateral migration of methane plays a role in the vicinity of the crest. The uniform distribution of hydrate in the flank of the ridge is an indication that flow in the flank could be predominantly one-dimensional.

The results of this study suggest that one-dimensional flux is dominant in the flank region of the ridge where hydrate concentrations are relatively constant. Near the crest of the ridge, lateral flow could play an increasing role. Lateral transport could take

place beneath the HSZ in high permeability gas filled regions which are covered by low permeability layers.

B. Chapter 4 Figure Captions

Figure 4.1

Pressure estimated at top and bottom of HSZ. The depth is calculated in the three-layer slowness gradient model and the pressure includes the water column, thin sediment layer, and HSZ (with an averaged porosity of 60%).

Figure 4.2

Phase equilibrium curve for hydrate in seawater from Peltzer and Brewer (2000) with temperature profile for site 997 from Wood and Ruppel (2000). The maximum and minimum pressures correspond to those values at the bottom of the HSZ in Figure 4.1. The overlap suggests that the bottom of the HSZ is consistent with the hydrate-gas phase boundary.

Pressure

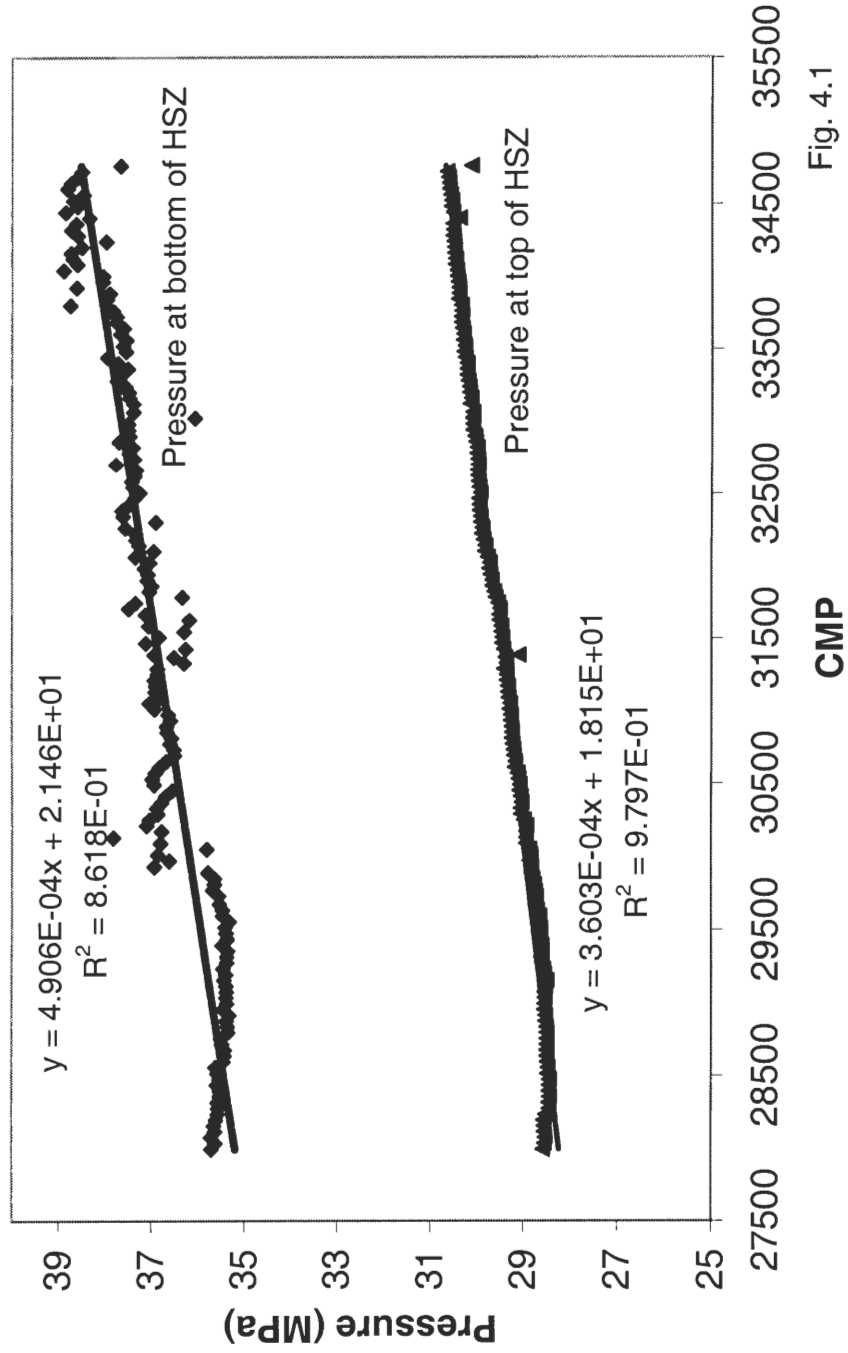


Fig. 4.1

Phase Boundary

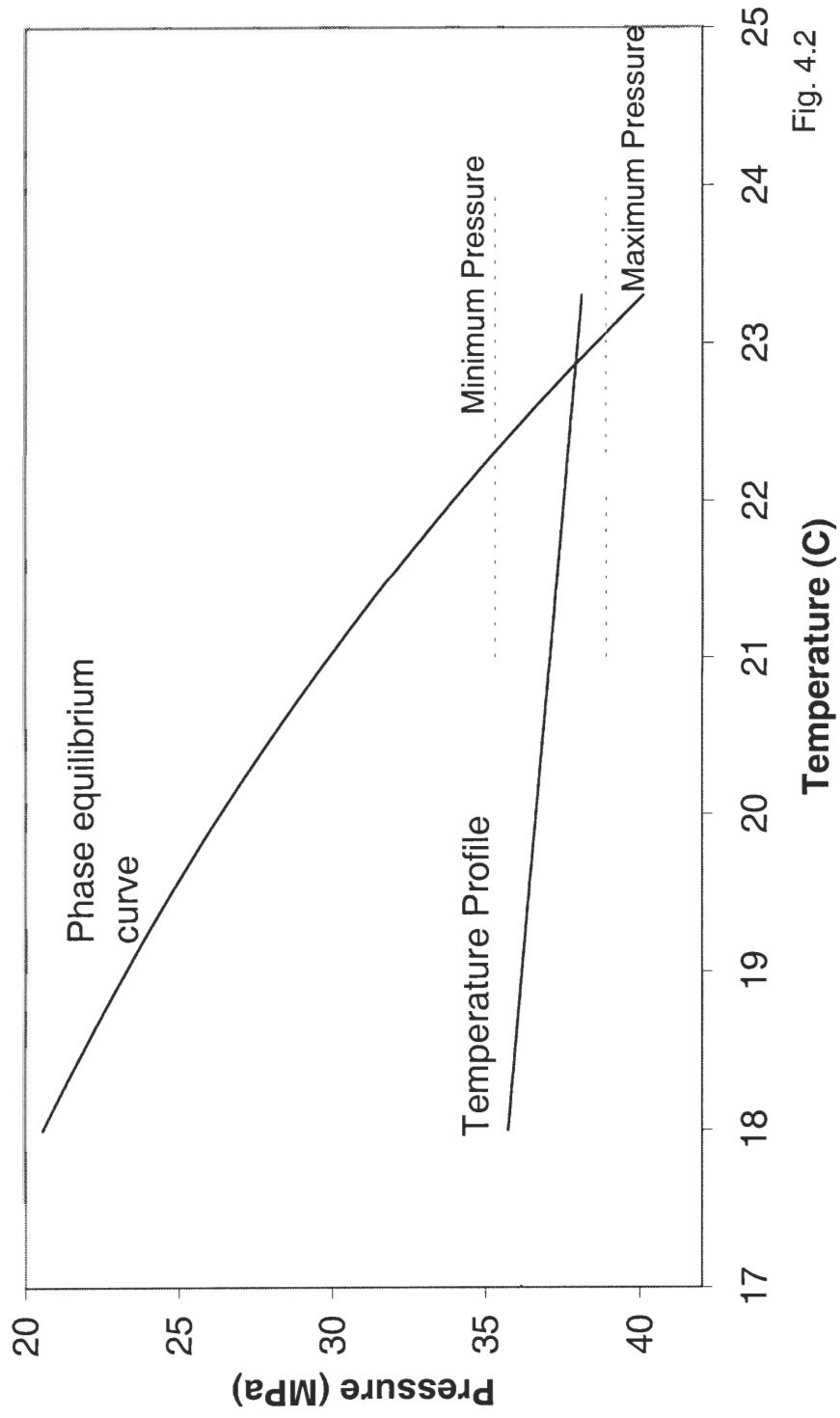


Fig. 4.2

Chapter 5

Conclusions

From the models that we have used to analyze the MCS data from Line R22, several conclusions can be drawn:

- a) The thickness of the HSZ (and HSZ') increases with distance from the crest. While the overall change is less than 10% of its magnitude, the understanding of the increase may shed light on the hydrate distribution.
- b) The sediment layer thins towards the flank. This result is consistent our understanding of how the ridge was formed; the rate of sediment deposition is greater near the crest.
- c) When the line is examined in the vicinity of the crest, significant changes of velocity with position are calculated. In the flank, there is no significant trend of velocity with position.
- d) Lateral migration of methane may play a more significant role in the crest region than it does in the flank where vertical flux is expected to dominate.

The role of methane in the global carbon cycle supports the need for further studies of methane flux. Among the questions that need to be addressed are: a) What are the characteristics of methane flux beyond the section studied? b) Is the rate of lateral flux constant with time, decreasing (after the formation of hydrate), or cyclic (coinciding with episodic collapses)? c) Are the vertical flow mechanisms dependent on the distance from the ridge?

References

- Beals, R.E. (1972). *Statistics: an introduction*. Rand McNally & Co., Chicago, 420 pages.
- Brooks, J.M., Anderson, A.L., Sassen, R., Macdonald I.R., Kennicutt II, M.C., and Guinasso, Jr, N.L. (1994). Hydrate Occurrences in Shallow Subsurface Cores by Continental Slope Sediments, in Sloan, E.D., Jr., Happel, John, and Hnatow, M.A., eds., *International Conference on Natural Gas Hydrates: Annals of the New York Academy of Sciences*, v. 715, p.381-391.
- Brown, L.B, Amos, J.R., and Mink, G.M. (1975). *Statistical Concepts*. Harper and Row, New York, 147 pages.
- Bugge, T. , Befring, S., Belderson, R. H., Eidvin, T., Jansen, E., Kenyon, N. H., Holtedahl, H.,and Sejrup, H.-P.(1987). A giant three-stage submarine slide off Norway. *Geo-Marine Letters*, 7, 191-198.
- Carson, B., Westbrook, G.K., Musgrave, R.J., and Suess, E. (Eds.) (1995). *Proc. ODP, Sci.Results*, 146 (Pt 1)
- Collett, T.S. and Ladd J. (2000). Detection of gas hydrate with downhole logs and assessment of gas hydrate concentrations (saturations) and gas volumes on the Blake Ridge with electrical resistivity log data, In: Paull, C.K., Matsumoto, R., Wallace, P.J., & Dillon, W.P. (eds). *Proceedings of the Ocean Drilling Program Scientific Results 164*, 179-191.
- Davie, M. K and Buffet, B. A. (2001). A numerical model for the formation of gas hydrate below the seafloor, *Journal of Geophysics. Res.*, v. 106 B1, AGU, pp. 497-514.
- Dickens, G.R., Paull, C.K., Wallace, P., and the ODP Leg 164 Scientific Party. (1997). Direct measurement of in situ methane quantities in a large gas-hydrate reservoir: *Nature*, v. 385, 426-428.
- Dickens, G.R. (2001). Modeling the global carbon cycle with a gas hydrate capacitor: significance for the latest Paleocene thermal maximum, in *Natural Gas Hydrates: Occurrence, Distribution, and Detection*. Geophysical Monograph 124, C.K. Paull and W.P. Dillon, eds., American Geophysical Union, pp. 19-40.
- Dillon, W.P., and Paull, C.K. (1983). Marine gas hydrates, II. Geophysical evidence, in Cox, J.S., ed., *Natural Gas Hydrates: Properties, Occurrences, and Recovery*, Butterworth Publishing, London, England, 73-90.
- Dillon, W.P. (1992). U.S. Geological Survey Marine and Coastal Geology Program, <http://marine.usgs.gov/fact-sheets/gas-hydrates/title.html>.

- Dillon, W.P. (1998). Gas hydrate as a potential resource - what do we need to know?: Methane Hydrates, International Symposium, Resource in the Near Future? Proceedings, Panel Discussion papers, Chiba City, Japan, October 1998, p. 13-15.
- Dillon, W.P., Danforth, W.W., Hutchinson, D.R., Drury, R.M., Taylor, M.H. and Booth, J.S.(1998). Evidence for faulting related to dissociation of gas hydrate and release of methane off the southeastern United States, *in* Henriot, J.P., and Mienert, J., eds., Gas Hydrates--Relevance to World Margin Stability and Climate Change: Geological Society of London, Special Publication, v. 137, p. 293-302.
- Ecker, C., Dvorkin, J., and Nur, A. (2001). Estimating the amount of gas hydrate and free gas from marine seismic data, *Geophysics*, 65, 565-573.
- Gorman, A.R., Holbrook W.S., Hornbach M.J., Hackwith K.L., Lizarralde, D, and Pecher, I.A. (2002). Rapid gas migration through the hydrate stability zone on the Blake Ridge, *Geology*, v. 30, p. 327-330.
- Helgerund, M.B, Dvorkin, J., Nur, A., Sakai, A., and Collett, T. (1999). Elastic-wave velocity in marine sediments with gas hydrates: effective medium modeling, *Geophysical Research Letters*, 26, 2021-2024.
- Helgerud, M.B.(2001). Wave speeds in gas hydrate and sediments containing gas hydrate: a laboratory and modeling study. Dissertation, Stanford University.
- Holbrook, W.S., Hoskins, H., Wood, W.T., Stephen, R.A., Lizarralde, D., and the ODP Leg 164 Party. (1996). Methane hydrate and free gas on the Blake Ridge from vertical seismic profiling, *Science* v.273, 1840-3.
- Holbrook, W.S.(2001). Seismic Studies of the Blake Ridge Hydrate Province: Implications for Hydrate Distribution, Methane Expulsion and Free Gas Dynamics, in *Natural Gas Hydrates: Occurrence, Distribution, and Detection*, Geophysical Monograph 124, C.K. Paull and W.P. Dillon, eds., American Geophysical Union, pp. 235–256.
- Hornbach, M J, Holbrook, W S, Gorman, A R, Hackwith, K L, Lizarralde, D, and Pecher, I A.(2003). Direct seismic detection of methane hydrates on the Blake Ridge. *Geophysics* v. 68(1) 92-100.
- Hunt, J.M. (1979). *Petroleum Geochemistry and Geology*, Freeman & Co., San Francisco, 617 pages.
- Hyndman, R.D., and Spence, G.D. (1992). A seismic study of methane hydrate marine bottom simulating reflectors, *Journal of Geophysical Research*, 97, 6683-6698.
- Hyndman, R., Spence G.D., Chapman R., Riedel M., Edwards R.N. (2001). Geophysical

studies of marine gas hydrates in northern Cascadia, AGU Gas Hydrates Monograph 124, 273-295.

Jeffrey, G.A. and McMullan, R.K. (1967). *Prog. Inorg. Chem.*, 8, 43.

Katzman, R., Holbrook, W. S., and Paul, C. K. (1994). Combined vertical-incidence and wide angle seismic study of a gas hydrate zone, Blake Ridge: *J. Geophys. Res.*, 99, 17975-17995.

Korenaga, J., Holbrook, W.S., Singh, S.C., Minshull, T.A. (1997). "Natural gas hydrates on the Southeast U.S. margin: Constraints from full waveform and traveltime inversions of wide-angle seismic data," *J. Geophys. Res.*, v. 102, p. 15,345–15,365.

Kvenvolden, K. A.(1993). Gas hydrates—geological perspective and global change, *Rev. Geophys.*, 31, 173–187.

Kvenvolden, K.A. (1993). Gas hydrates as a potential energy resource -- a review of their methane content, in Howell, D.G., ed., *The Future of Energy Gases: U.S. Geological Survey Professional Paper 1570*, p. 555-561.

Kvenvolden, K.A. (1995). A review of the geochemistry of methane in natural gas hydrate, *Org. Geochem.*, 23, 997-1008.

Kvenvolden, K.A. and Lorenson, T.D. (2001). The global occurrence of natural gas hydrate, in *Natural Gas Hydrates: Occurrence, Distribution, and Detection*, Geophysical Monograph 124, C.K. Paull and W.P. Dillon, eds., American Geophysical Union, pp. 3-15.

Laberg, J. S., Vorren, T. O., Dowdeswell, J. A., Kenyon, N. H., and Taylor, J. (2000). The Andoya slide and the Andoya canyon, north-eastern Norwegian-Greenland Sea. *Marine Geology*, 162, 259-275.

Lee, M.W., Hutchinson, D.R., Collett, T.S., and Dillon, W.P. (1996). Seismic velocities for hydrate-bearing sediments using weighted equation. *J. Geophys. Res.*, 101:20347-20358.

Masters, C.D., Root, D.H., and Attanasi, E.D. (1991). Resource constraints in petroleum production potential: *Science*, v. 253, 146-152.

Miller, J.J., Lee, M.W., and von Huene. (1991). An analysis of seismic reflection from the base of a gas hydrate zone, offshore Peru, *AAPG Bulletin*, 75, 910-924.

Mountain, G.S. and Tucholke B.E. (1985). Mesozoic and Cenozoic Geology of the U.S. Atlantic Continental Slope and Rise, in C.W. Poag (ed). *Geologic Evolution of the United States Atlantic Margin*.

- Nisbet, E., and Piper, D. W. (1998). Giant submarine slides. *Nature*, 392, 329-330.
- North, F. K. (1985). *Petroleum Geology*, Allen & Unwin, Inc., Winchester, MA.
- Paull, C.K., Ussler, W., III, and Borowski, W.A. (1994). Sources of biogenic methane to form marine gas-hydrates: in situ production or upward migration? *Ann. N.Y. Acad. Sci.*, 715:392-409.
- Paul, C. K., R. Matsumoto, Wallace, P. J., et al. (1996). *Proc. ODP, Init. Repts.*, 164, College Station, TX (Ocean Drilling Program).
- Paull, C.K. and Matsumoto, R. (2000). Leg 164 Overview, in *Proc. ODP, Sci. Results 164*, edited by C.K. Paull, R. Matsumoto, P.J. Wallace, and W.P. Dillon, Ocean Drilling Program, College Station Texas.
- Peltzer, E. T. and Brewer P.G. (2000). Practical physical chemistry and empirical predictions of methane hydrate stability. In: M.D. Max (ed.), *Natural Gas Hydrate in Oceanic & Permafrost Environments*. Kluwer Academic Publishers, Netherlands.
- Redfield, A.C., Ketchum, B.H., and Richards, F.A. (1963). The influence of organisms on the composition of seawater. In *The Sea*, Vol. 2, (Ed. M.N. Hill), pp 26-79. Wiley Interscience: New York.
- Rempel, A.W. and Buffet, B.A. (1997). Formation and accumulation of gas hydrate in porous media, *J. Geophys. Res.*, 102, 10,151-10.
- Shipley, T. H., Houston, M. H., Buffler, R. T., Shaub, F. J., McMillen, K. J., Ladd, J. W., and Worze., J. L. (1979). Seismic reflection evidence for widespread occurrence of possible gas-hydrate horizons on continental slopes and rises: *AAPG Bull.*, 63, 2204-2213.
- Singh, S.C. and Minshull, T.A. (1994). Velocity structure of a gas hydrate reflector at Ocean Drilling Program Site 889 from global seismic waveform inversion, *J. Geophys. Res.*, 99, 24,221-24,233, 1994.
- Sloan, E.D. (1990, 1998). *Clathrate Hydrates of Natural Gas*, 1st & 2nd Ed., Marcel Dekker, New York, 705pp.
- Sloan E.D., Brewer P.G., Collett, T.S., Dillon, W.P., Holbrook, W.S., Kvenvolden, K.A., Paull, C.K. (1999). "A Gas Hydrate Research Program" <http://www.mines.edu/research/chs/plan.html>.
- Taylor, M., Dillon, W., Anton, C., and Danforth, W. (1999). Seismic reflection surveys of the Blake Ridge, R/V Cape Hatteras 1992 and 1995: Data acquisition, navigation and processing, U.S. Geological Survey Open File Report 99-372.

- Tissot, B.P., and Welte, D.H. (1984). Petroleum formation and occurrence: Berlin, Springer-Verlag, 699 pgs.
- Wood, W.T. and Ruppel, C. (2000). Seismic and thermal investigations of the Blake Ridge gas hydrate area: a synthesis, Proc. of ODP, Scientific Reports, Leg 164, 253-264.
- Wood, W.T., and Gettrust, J.F. (2001). Deep-tow seismic investigations of methane hydrates, in Natural Gas Hydrates: Occurrence, Distribution, and Detection, Geophysical Monograph 124, C.K. Paull and W.P. Dillon, eds., American Geophysical Union, pp. 165-177.
- Xu, W. and Ruppel, C. (1999). Predicting the occurrence, distribution, and evolution of methane gas hydrate in porous marine sediments, J. Geophys. Res., 104, 5081-5096.

Vita

Daniel Kahn was born in Charlottesville, Virginia and grew up in South Kingstown, Rhode Island. He graduated with high honors from South Kingstown High School in 1997. Dan attended Brown University and graduated with honors (Sc.B.) in May 2001, completing a concentration in Geology-Physics/Mathematics. His Senior Honors Thesis was titled: *El Nino Activity and the Production of Chlorophyll: A case study of phytoplankton production near the Southern Californian Coast, 1997-2000*. While at Brown, he was a University Teaching and Research Assistant (UTRA) and a Space Grant Award Recipient. He also interned at Williams Corporation in Tulsa, Oklahoma, where he worked on the Energy Trading Floor. Since August 2001, Dan has been a graduate student at Georgia Institute of Technology.